学位論文

Cation Ordering and Electrical Properties of Double Perovskite Molybdate Thin Films

（二重ペロブスカイト型 Mo 酸化物薄膜における カチオン配列と電気物性の研究）

平成 26 年 12 月博士（理学）申請

東京大学理学系研究科化学専攻

重松　圭

Cation Ordering and Electrical Properties of Double Perovskite Molybdate Thin Films

by

Kei Shigematsu

Department of Chemistry
Graduate School of Science
The University of Tokyo
December, 2014

Abstract

Transition-metal oxides with double-perovskite structure $A_2BB'O_6$ are known to exhibit a variety of electronic properties, such as room temperature magnetoresistance in Sr_2FeMoO_6 and magnetodielectric properties in La_2NiMnO_6, depending on the combination of *B*- and *B*'-site cations. Among them, Sr_2MgMoO_6 (SMM) has attracted much attention as a promising anode material for hydrocarbon-fueled solid-oxide fuel cells (SOFCs), because of its high tolerance to carbon deposition and sulfur poisoning, which enables the direct use of natural gas fuel instead of hydrogen.

An important influence on the performance of anode materials in fuel cells is electrical conductivity. Although stoichiometric SMM with d^0 Mo^{6+} is a typical insulator, SMM tends to contain oxygen vacancies ($Sr_2MgMoO_{6-\delta}$) at high temperatures under reductive atmospheres, which are the typical working conditions for SOFC anodes. Because of this, the oxygen-vacant SMM conducts current because of the mixed valence state of Mo^{5+} and Mo^{6+}. However, the conductivity of SMM did not meet the practical requirement under typical operating conditions. One central reason for the poor ρ is that the amount of oxygen vacancies in SMM is limited to $\delta = 0.046$, so long as SMM is synthesized by a conventional solid-state reaction at equilibrium, although δ increases as *B*-site ordering ratio decreases. In bulk SMM, the Mo ions favor the hexavalent state and tend to be ordered alternately with Mg^{2+}, due to the large difference in their ionic charges. Thus, the use of a non-equilibrium synthetic approach might further increase Mg/Mo disorder and enhance δ, beyond the limitation imposed by conventional solid-phase reactions.

In this study, I have fabricated oxygen-vacant SMM thin films by pulsed laser deposition (PLD), which enables the growth of thin films in non-equilibrium conditions because of the large kinetic energies of ablated plumes. As a result, I achieved the

fabrication of epitaxial thin films of SMM containing a sizable amount of oxygen vacancies, depending on the substrate temperature and oxygen partial pressure during PLD growth. I also investigated crystal structure, electronic states, and electric properties of SMM thin films. X-ray diffraction revealed that extensive *B*-site disorder was introduced into the SMM films. The resistivities of SMM films on $SrTiO_3$ (111) substrate were remarkably low, within the range of $2.7-6.6 \times 10^{-2}$ Ω cm at 300 K, and systematically correlated with the ordering ratio and δ values estimated from the Mo 3*d* photoemission spectra. I concluded that the difference in conductivity among various samples is due to the variation of the amount of oxygen vacancies. This study demonstrates the possibility to improve the properties of "ordered" double perovskites by introducing disorder in *B*-sites.

List of abbreviations and symbols

DOS	density of states
f.u.	formula unit
FWHM	full-width half-maximum
HAXPES	hard x-ray photoemission spectroscopy
PLD	pulsed laser deposition
RHEED	reflection high energy electron diffraction
SOFC	solid state fuel cell
SMM	$Sr_2MgMoO_{6-\delta}$
VRH	variable range hopping (model)
XRD	x-ray diffraction/diffractometry
XPS	x-ray photoemission spectroscopy

AS	antisite parameter
d	distance between lattice planes
D	Debye-Waller factor
E_B	binding energy
E_F	Fermi energy
I	spectrum intensity
f	atomic scattering factor
h, k, l	Miller indices
L	Lorentz factor
N	absorption factor
p	polarization factor
P_{O2}	oxygen partial pressure
R	ordering ratio
T_s	substrate temperature
$\theta, \omega, \chi, \phi$	rotating angles in XRD
δ	oxygen vacancy parameter
ρ	resistivity
λ	wavelength

Contents

Chapter 1 General Introduction

1.1 Double perovskite oxides

Perovskite materials, with a chemical formula of ABO_3, have attracted much attention because of a huge variety of intriguing electronic properties derived from the interplay between charge, spin, and orbital degrees of freedom. The *A*-sites of perovskite are occupied by cations with larger ionic radii such as rare-earth or alkali-earth metals, and the *B*-sites are occupied by cations with smaller ionic radii such as transition-metals.

Double perovskite, with a chemical formula of $A_2BB'O_6$, is a subclass of perovskite that results from half replacement of *B* ion by different *B*' ion in ABO_3 [1]. Double perovskite contains two different octahedral, BO_6 and $B'O_6$, with a molar ratio of 1:1, resulting in the appearance of additional features, such as structural flexibility and ordering of *B*-site ions. There are several ways for *B*-cation arrangements in double

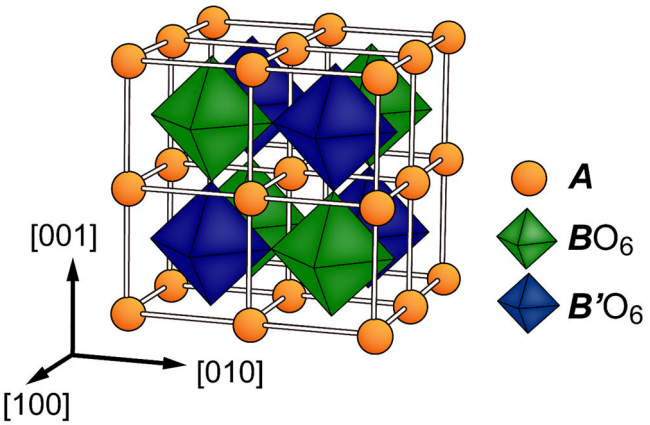

Figure 1-1. Schematic illustration of double perovskite $A_2BB'O_6$ with rock-salt type order.

perovskites: perfect disorder, rock-salt type, columnar, and layered ordering. The disorder phase implies that *B* and *B*' ions occupy randomly in the center of BO_6 octahedral. Meanwhile, the latter three phases exhibit regular arrangements of *B*/*B*' ions. The columnar and layered type are rarely realized and only few examples are known (See ref. [1]). In contrast, the rock-salt type ordering is the most widely observed pattern in double

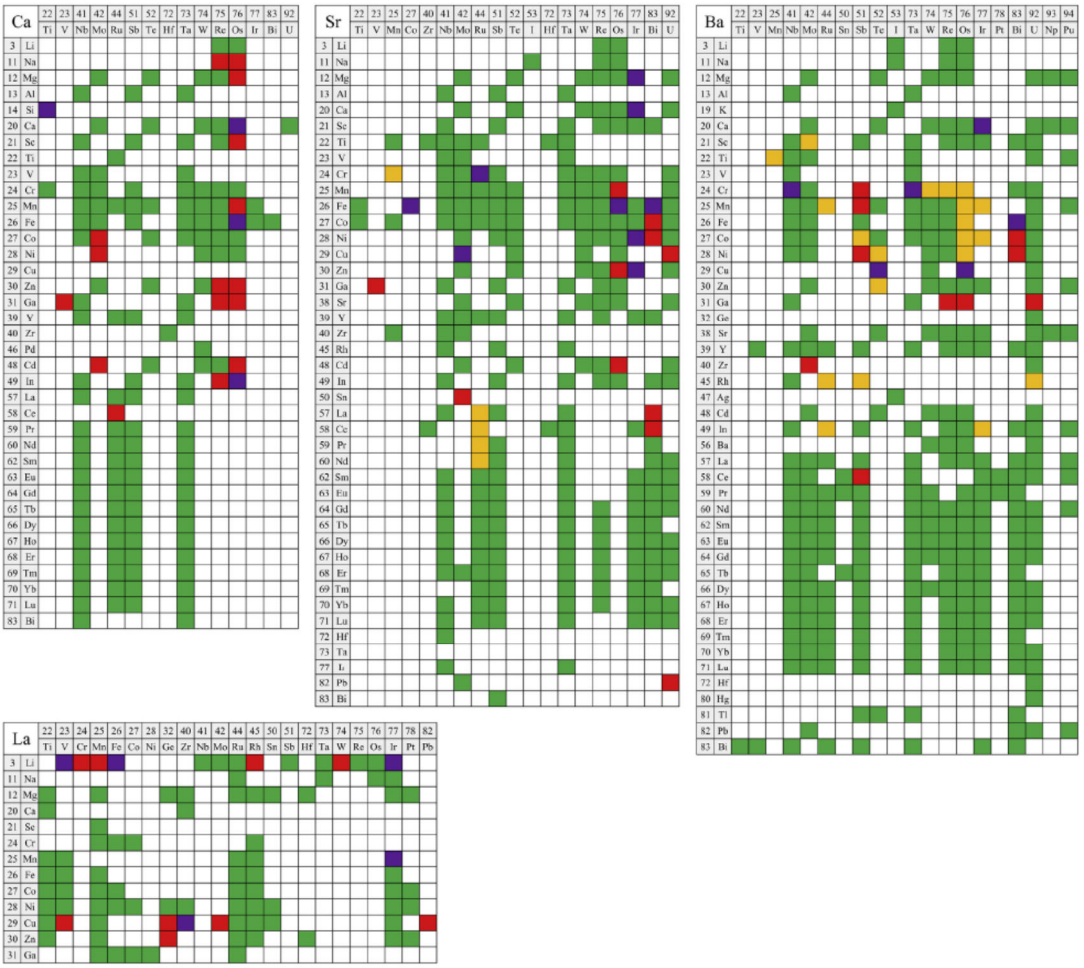

Figure 1-2. A_2BBO_6 compositions with *A* = Ca, Sr, Ba or La reported to date. The colors indicate synthesized conditions: at ambient pressure (green), stabilized using either high-pressure or high oxygen-partial-pressure synthesis (purple), and not double perovskite (other colors). Reprinted from [69] Copyright 2015, with permission from Elsevier.

perovskites. To date, more than 720 compounds were reported, as reviewed in Fig. 1-2 [69].

Anderson *et al.* surveyed more than 200 double perovskite compounds and found that the differences in charge and ionic radii influenced the *B*-site arrangements [2]. When the differences in charge and ionic radii are both small, the *B*-site ions tend to arrange in a disordered manner. In contrast, when the differences are both large enough, the rock-salt type ordering tends to appear. In addition, there is an intermediate region between these two phases, in which *B*-site arrangement can be controlled by tuning the synthesis condition. This rule is visualized in Fig. 1-3. This simple rule based on ionic charge and radii is practically useful for predicting which phase is facile in bulk form.

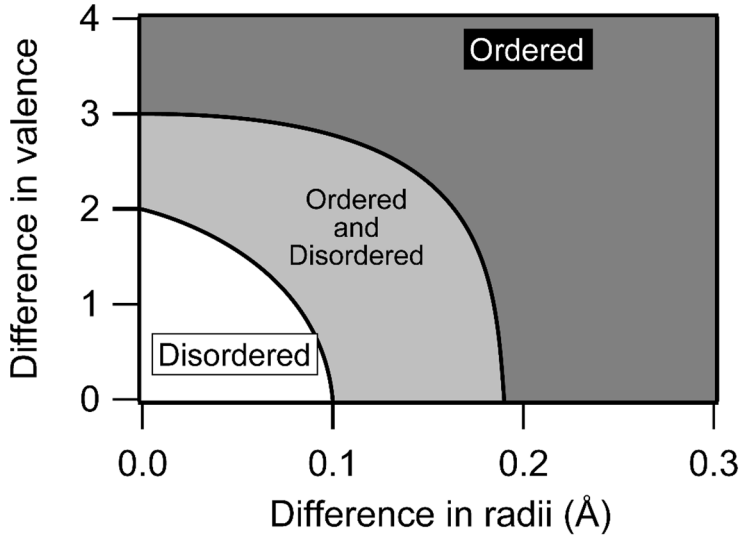

Figure 1-3. Phase diagram of *B*-site ordering patterns as a function of the differences in valence and radii between two *B* and *B*' sites. (Adopted from [2] and [3]).

In many double perovskites, the extent of ordering (R) critically affects their physical properties. For example, double perovskite Sr_2FeMoO_6 shows half-metallic ferrimagnetism in ordered phase, but this property degrades sensitively as R decreases (details reviewed later)[4]. In order to discuss how physical properties depend on the extent of ordering, it is useful to employ the parameter of antisite (AS), which is defined as the fraction of misplaced B cation in B' site and *vice versa*. Then, the relationship between the extent of ordering R and AS can be described as

$$R = 1 - 2AS.$$

Ordering ratio can be evaluated by x-ray diffraction measurement as mentioned in experimental chapter. Investigating the relationship between R and physical properties is a central issue for double-perovskite studies.

1.2 Ordering control and properties of double perovskite

In this section, I briefly review some representative examples of double perovskites whose physical properties are influenced by *B*-site ordering. These examples suggest an importance of controlling ordering ratio and physical properties.

Sr_2FeMoO_6

Sr_2FeMoO_6 is one of the most intensively studied double perovskite compounds due to its half-metallicity with Curie temperature above room temperature [4]. The ideal magnetic moments of Sr_2FeMoO_6 is 4 μ_B per fourmla unit (f.u.) arising from antiferromagnetic coupling between Fe^{3+} (S = 5/2) and Mo^{5+} (S = 1/2). However, it had been pointed out since the early stage that the *B*-site ordering ratio is very sensitive to synthesis conditions, as is consistent with the phase diagram of Fig. 1-3, and influenced magnetization and half-metallicity in Sr_2FeMoO_6. For example, *AS* at the Fe and Mo site showed linear dependence with the saturation magnetization (~ 3.6 μ_B/f.u.) and the low field magnetoresistance in bulk Sr_2FeMoO_6 [5,7]. Note that the magnetoresistance is caused by tunneling of spin-polarized carriers from half-metallic Sr_2FeMoO_6 through surface barriers (e.g. $SrMoO_4$) [6]. Some computational studies including Monte Carlo simulation [8] and *ab initio* band-structure calculation [9] reproduced the above mentioned tendency.

The thin-film growth of half-metallic material is an inevitable step toward fabrication of spintronic devices. Thus, pulsed laser deposition (PLD) or sputtering growth conditions for Sr_2FeMoO_6 have been extensively investigated compared to other double

perovskite materials. For example, Manako *et al.* reported that high-quality Sr_2FeMoO_6 film can be obtained near a crossover point between two oxidation states in the phase diagram as shown in Fig. 1-4, which suggested that thermodynamics of constituent element was an important factor [10]. Shinde *et al.* reported that *B*-site ordered Sr_2FeMoO_6 film can be obtained only when the substrate temperature is set above 900°C during deposition [11]. Their ordered films showed magnetic properties (saturation magnetization ~3.28 μ_B/f.u.) comparable to those of bulk samples. Kadota *et al.* indicated that the environmental pressure affected the formation of secondary phases: $SrMoO_4$ in an oxidative condition and Fe metal in a reductive condition [12]. Findings based on many studies including above-mentioned now enable to fabricate Sr_2FeMoO_6 thin films of a quality as high as polycrystalline one. For example, Hauser *et al.* fabricated phase-pure and highly ordered (R ~ 0.85) Sr_2FeMoO_6 film on $SrTiO_3$ (111) substrate by carefully controlling the stoichiometry of Fe/Mo and by changing process gas (Ar, Ar+H_2 and Ar+O_2) pressure, and they achieved the direct observation of Fe/Mo ordering by transmission electron microscopy [13]. It was also revealed that excess Sr also degraded the magnetic properties due to the formation of extra SrO layers in the crystal [14].

In summary, the growth of *B*-site ordered and nearly half-metallic Sr_2FeMoO_6 thin films requires careful control of process conditions such as temperature and atmosphere. However, it is also remarkable that PLD and other thin-film growth processes provide the possibility of widely changing the extent of *B*-site ordering in double perovskite by controlling the growth conditions.

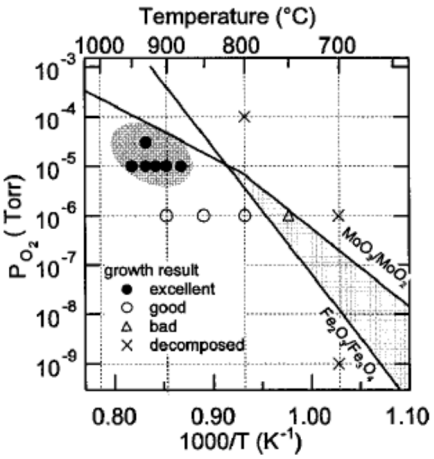

Figure 1-4. Sr_2FeMoO_6 films plotted in substrate temperature and oxygen partial pressure diagram. Thermodynamic boundaries of MoO_3/MoO_2 and Fe_2O_3/Fe_3O_4 are also displayed. Reprinted with permission from [10]. Copyright 1999, AIP Publishing LLC.

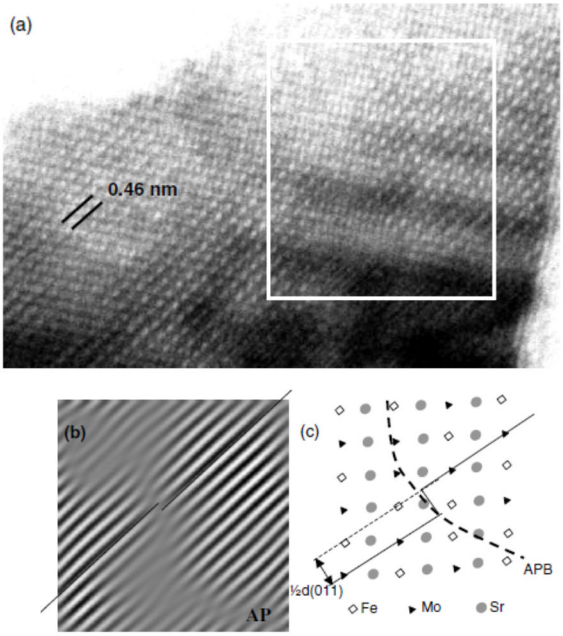

Figure 1-5. (a) High-resolution electron microscopy of Sr_2FeMoO_6 samples (b) Fourier reconstructed image of the boxed area in (a). Obscure region indicates *B*-site disorder. (c) Schematic illustration of the atomic structure. Broken line indicates anti phase boundary (APB). [7] (c) IOP Publishing.

La_2NiMnO_6

There have been many researches searching for multiferroic materials in which ferromagnetism and electrical polarization are coupled with each other at room temperature. One of the attracting candidates is R_2NiMnO_6 where R is a rare-earth element). La_2NiMnO_6 exhibited Curie temperature near room temperature (T_C = 287 K for R = La). It is predicted that R_2NiMnO_6 has potential to show multiferroelectricity by tuning chemical pressure and/or epitaxial strain [15]. La_2NiMnO_6 is also known to exhibit ferromagnetic insulator, and considered as a candidate of spin filter materials which have spin-dependent tunneling probability due to spin-dependent potential barrier height. Because of this, the material is suitable for barrier layer in tunnel magnetoresistance devices [16−20]. Note that all these properties, i.e., Curie temperature near room temperature, significant electric polarization, and spin-filter behavior, are sharply degrade with decreasing the extent of *B*-site ordering.

PLD growth conditions for La_2NiMnO_6 have been studied from the viewpoint of controlled *B*-site ordering. Hashisaka *et al.* reported that oxygen partial pressure during deposition significantly affected the *B*-site ordering and that oxidative conditions are necessary to stabilize the ordered state, judging from the magnetization (Fig. 1-6) [17]. Singh *et al.* investigated wider PLD conditions as shown in Fig. 1-7 and confirmed long-range order. They reported that ordered and disordered La_2NiMnO_6 can be synthesized selectively [21]. In addition, comparison of the film on $SrTiO_3$ and $(LaAlO_3)_{0.3}$-$(SrAl_{0.5}Ta_{0.5}O_3)_{0.7}$ substrates revealed that migration process on the substrate in the initial growth stage influenced to the *B*-site ordering in La_2NiMnO_6 [22].

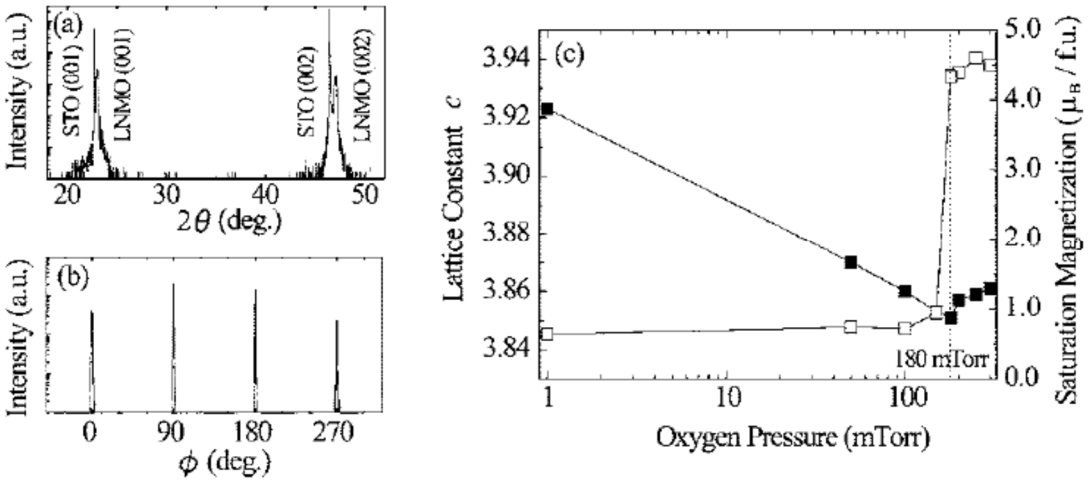

Figure 1-6. (a) Out-of-plane x-ray diffraction pattern and (b) ϕ scan of in-plane 200 reflections of the heteroepitaxial La_2NiMnO_6/STO (001) film. (c) Out-of-plane lattice constant (black squares) and magnetization at 5 K (open circles) as a function of oxygen partial pressure during PLD deposition. Reprinted with permission from [17]. Copyright 2006, AIP Publishing LLC.

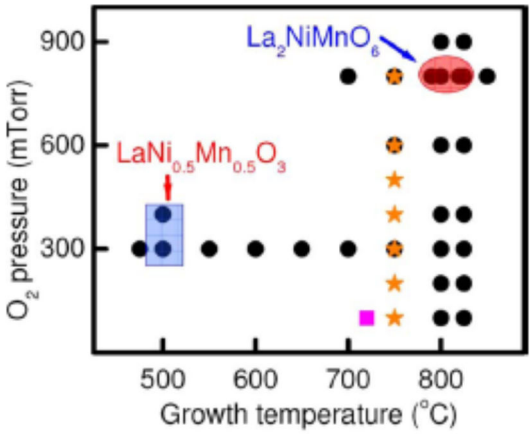

Figure 1-7. Substrate-temperature and oxygen partial pressure diagram of La_2NiMnO_6. The optimum conditions for ordered and disordered La_2NiMnO_6 were surrounded by red circle and blue square, respectively. Reprinted figure with permission from [21], Copyright 2009 by the American Physical Society.

La_2CrFeO_6 and some "disordered" double perovskites

Recently, some *B*-site ordered double perovskites, which belongs to "disordered" phase, have been successfully synthesized.

A typical example is La_2CrFeO_6, where Cr^{3+} and Fe^{3+} are isovalent and have similar ionic radii, and thus spontaneous *B*-site ordering is not expected. This material was predicted to show ferromagnetism based on $3d^3$-$3d^5$ configuration according to Kanamori-Goodenough rule [23,24]. Chakraverty *et al.* succeeded in fabricating highly ordered La_2CrFeO_6 thin films on $SrTiO_3$ (111) substrate [25]. They showed that the ordered La_2CrFeO_6 thin films can be obtained in a narrow window of PLD conditions as shown in Fig 1-8(a). The best samples showed ~2 μ_B/f.u. of net magnetization, suggesting antiferromagnetic Fe-Cr interaction (Fig.1-8 (b), (c)). This cannot be explained by Kanamori-Goodenough rule but is consistent with the result of local spin-density calculation [26].

Another example is Sr_2TiRuO_6, where Ti^{4+} and Ru^{4+} are isovalent and ionic radii difference is smaller than 0.02Å. However, Sr_2TiRuO_6 thin film with high *B*-site ordering was also obtained on $SrTiO_3$ (111) substrate by PLD [27]. As the extent of *B*-site order increased, the resistivity became larger because carrier localization became stronger (Fig. 1-9).

The *B*-site ordered phase of "disordered" double perovskites have also been achieved in La_2VMnO_6 [28] and $LaSrVMoO_6$ [29] by PLD. These studies indicate great potential of PLD to control the *B*-site order of double perovskites beyond thermal equilibrium.

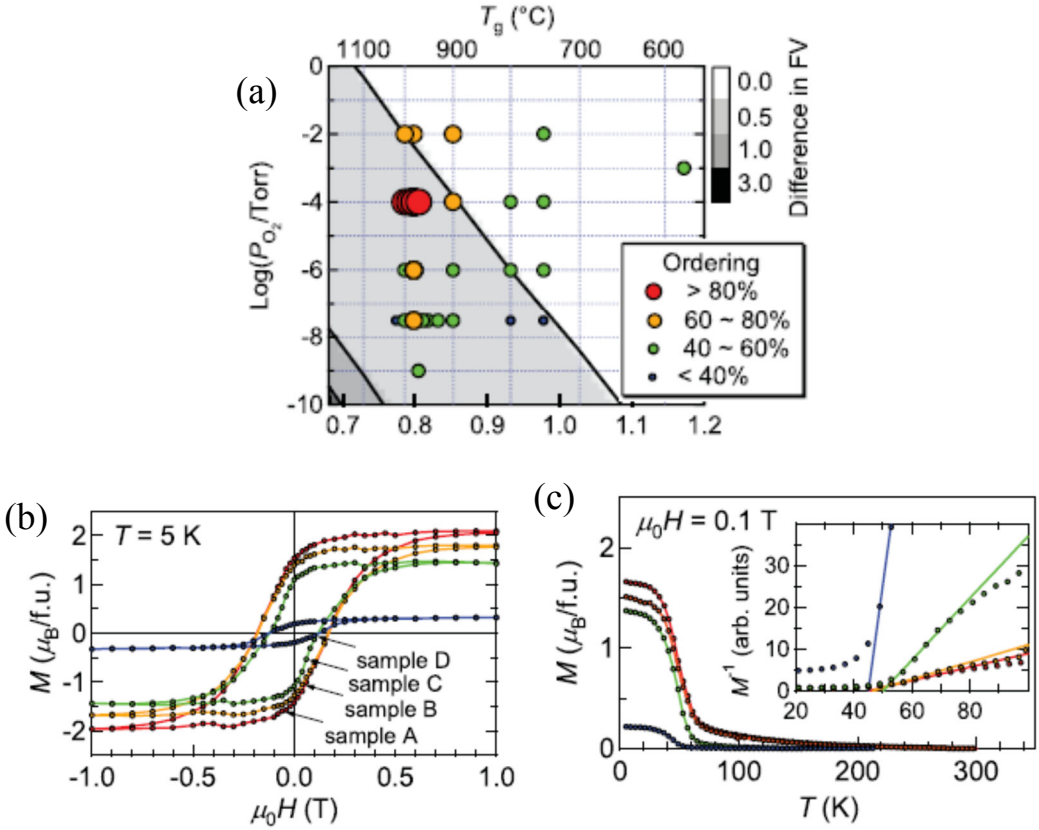

Figure 1-8. (a) Oxygen partial pressure and substrate temperature dependence of *B*-site order. Circle size and color indicate the extent of order. (b) Magnetization hysteresis curves for four different samples. Here the extent of ordering ratio is the highest in sample A and decreases in the order of B, C, and D. (c) The temperature dependence of magnetization. Inset shows the temperature dependence of inverse magnetization. Solid lines are linear fits to the plots above Curie temperature.

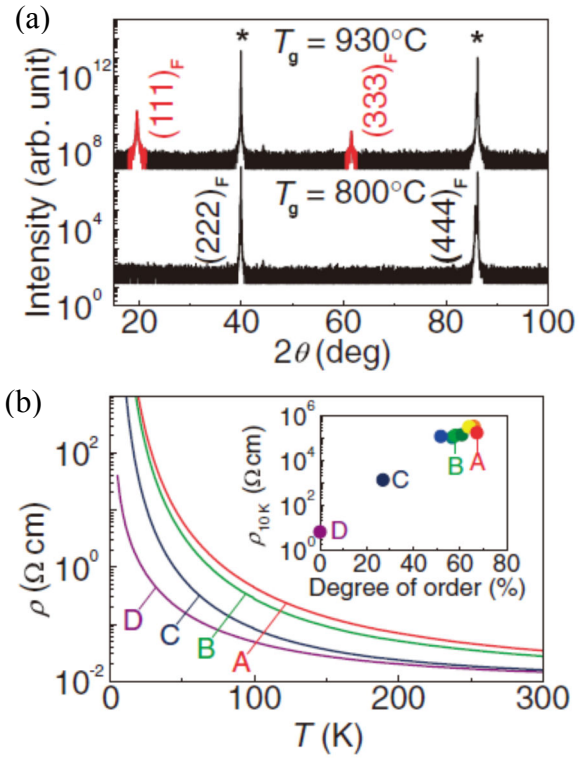

Figure 1-9. (a) XRD diffraction from ordered (top) and disordered (bottom) Sr_2TiRuO_6 thin films. (b) Resistivity vs. temperature plots for four different ordering ratio. [27]

1.3 Sr_2MgMoO_6

Sr_2MgMoO_6 (SMM) is the main target material in this study. Table 1-1 summarizes structural parameters of the constituent ions of SMM [30]. SMM belongs to "ordered perovskite" mainly due to the large difference in ionic valence between Mg^{2+} and Mo^{6+}. The unit cell of SMM is basically tetragonal at room temperature because of octahedral tilting [31], but it is convenient to use a pseudo-cubic cell.

SMM attracts much attention as a promising anode material for hydrocarbon-fueled solid-oxide fuel cells (SOFCs) [32, 33]. The strategy for finding SMM was explained in [32] as following two points: (1) the perovskite structure which possesses high electron/ion conduction like as a typical electrolyte of $La_{0.8}Sr_{0.2}Ga_{0.8}Mg_{0.2}O_{3-\delta}$, and (2) the ability of Mo^{6+}/Mo^{5+} which plays as a catalytic roll in SOFC anode without changing six-coordination in perovskite. The perovskite structure containing Mo^{6+}/Mo^{5+} requires the double perovskite structure with M^{2+} as a counter *B*-site cations due to charge balance. Then, fuel cell performances with Sr_2MMoO_6 with different M^{2+} was investigated. Figure 1-10 depicts the results of *M* = Mg and Mn. It is notable that SMM-anode cell maintained the power density in the presence of H_2S, while power density

Table 1-1. Structural parameters of the constituent ions of SMM [30].

Ionic valence	Coordination number	Shannon's ionic radii (Å)
Mg^{2+}	6	0.72
Mo^{6+}	6	0.59
Sr^{2+}	12	1.44

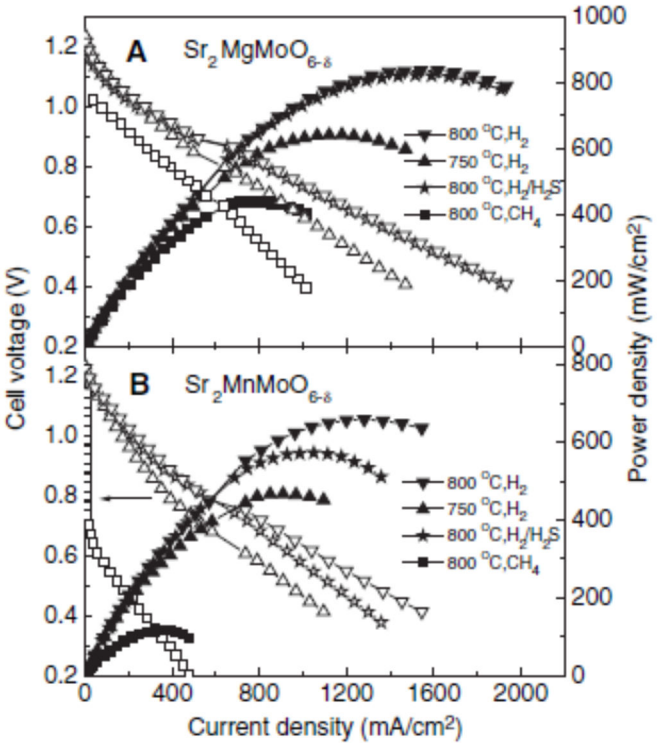

Figure 1-10. Fuel cell performance with anode of Sr_2MgMoO_6 (**A**) and $SrMnMoO_6$ (**B**) with fuel gas of H_2, H_2/H_2S and CH_4 [32]. Reprinted with permission from AAAS.

decreased in Sr_2MnMoO_6-anode cell. Moreover, SMM-anode cell exhibited large power generation when using CH_4 fuel gas. These results suggest that SMM possesses high tolerance to carbon deposition and sulfur poisoning, which enables the direct use of natural gas fuel instead of hydrogen in SOFCs [34−38].

Stoichiometric SMM with d^0 Mo^{6+} is a typical insulator, SMM tends to contain oxygen vacancies ($Sr_2MgMoO_{6-\delta}$) at high temperatures under reductive atmospheres, which are the typical working conditions for SOFC anodes. Because of this, the oxygen-vacant SMM conducts current because of the mixed valence state of Mo^{5+} and Mo^{6+}. However, SMM's conductivity, ρ, has been reported to fall between 10^{-1} and 10^{1} Ω cm even at 800°C, which does not meet the practical requirement of $\rho < 10^{-2}$ Ω cm under typical operating conditions [39]. Much efforts have so far been devoted to the

improvement of the electric conductivity of SMM. A typical way to obtain conducting SMM is efficient generation of Mo^{5+} via chemical doping, but actually significant improvement has not confirmed, as listed in Table 1-2.

Table 1-2. Resistivity of polycrystalline $Sr_2MgMoO_{6-\delta}$ and doped compounds.

Chemical Composition	Synthesis method	ρ (Ω cm) at 800°C	References
Sr_2MgMoO_6	Sol-gel method, 1200 °C (Ar+H_2)	0.1 – 0.2	[33]
Sr_2MgMoO_6	Freezing dry, 1000°C (Ar+H_2)	1.3	[40]
Sr_2MgMoO_6	Solid-state reaction, 1500°C (Air) → 800°C (Ar+H_2)	0.5	[41]
Sr_2MgMoO_6	Freezing dry 1200°C → 950°C (Ar+H_2)	5.3	[42]
$Sr_{1.4}La_{0.6}MgMoO_6$	sol–gel method, 1150°C (Ar+H_2)	0.13	[43]
$Sr_{1.4}Sm_{0.6}MgMoO_6$	Solid-state reaction, 1200°C (Ar+H_2)	0.063	[44]
$Sr_2Mg_{0.5}Fe_{0.5}MoO_6$	Solid state reaction 1200°C → 1000°C (Ar+H_2)	0.036	[45]
$Sr_2Mg_{0.95}Al_{0.05}MoO_6$	Solid state reaction, 1500°C (Air) → 1300°C (Ar+H_2)	0.19	[46]
$Sr_2Mg_{0.3}Co_{0.7}MoO_6$	Solid state reaction, 1500°C (Air) → 1300°C (Ar+H_2)	0.1	[47]
$Sr_2Mg(Mo_{0.5}Nb_{0.5})O_6$	Solid state reaction, 1500°C (Air) → 1000°C (Ar+H_2)	3.4	[41]
$Sr_2Mg(Mo_{0.6}W_{0.4})O_6$	Solid state reaction, 1200°C (Air) → 1000°C (Ar+H_2)	8.3	[41]

Another possible approach would be to find an efficient method for introducing oxygen vacancies in SMM. However, the amount of oxygen vacancies in SMM is limited to δ = 0.046 so long as SMM is synthesized by a conventional solid-state reaction at equilibrium, although δ increased as *B*-site ordering ratio decreased as seen in Fig. 1-11 [48].

This tendency can be explained by considering environment of oxygen anions in SMM crystal structure (Fig. 1-12). Mo ions favor the hexavalent state and tend to be ordered alternately with Mg^{2+}, due to the large difference in their ionic charges. In this ordered SMM, all of oxygen ions have a bond of Mg^{2+}–O^{2-}–Mo^{6+}. On the other hand, in disordered SMM, some oxygen ions bonded with two Mg^{2+}, i.e. Mg^{2+}–O^{2-}–Mg^{2+}, and another oxygen ions bonded with two Mo^{6+}, i.e. Mo^{6+}–O^{2-}– Mo^{6+}. Here the formation energy of oxygen vacancy $V_O^{\bullet\bullet}$ will be different between Mg^{+}–$V_O^{\bullet\bullet}$–Mg^{+}, Mg^{+}–$V_O^{\bullet\bullet}$–Mo^{5+}, Mo^{5+}–$V_O^{\bullet\bullet}$– Mo^{5+}, and Mo^{5+}–$V_O^{\bullet\bullet}$– Mo^{5+}. It is considered that Mo^{5+}–$V_O^{\bullet\bullet}$– Mo^{5+} is most favorable because the reduction of Mg and/or the formation of five coordination of Mg can be avoided. Note that similar idea has been proposed to explain the relationship between oxygen vacancy and disorder in Sr_2FeMoO_6 [49].

In short, introducing disorder in SMM creates the linkage of Mo–O–Mo which is preferable to generating oxygen vacancy, though disordered SMM is difficult to achieve. Here, the use of a non-equilibrium synthetic approach might further increase Mg/Mo disorder and enhance δ, beyond the limitation imposed by conventional solid-phase reactions.

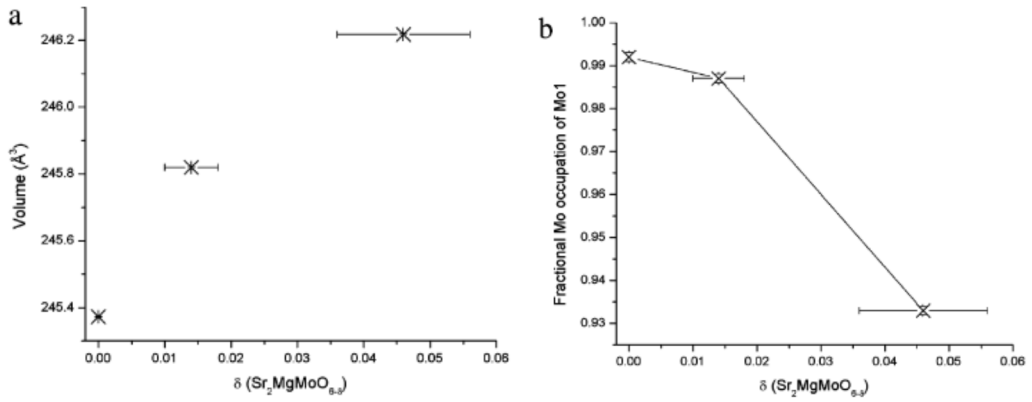

Figure 1-11. Cell volume and ordering parameter as a function of oxygen vacancies δ in polycrystalline $Sr_2MgMoO_{6-\delta}$. Note that the sample with largest $\delta = 0.046$ contained decomposed phase of $Sr_3(MgMo)O_{7-\delta}$. Reprinted with permission from [48] Copyright 2007 American Chemical Society.

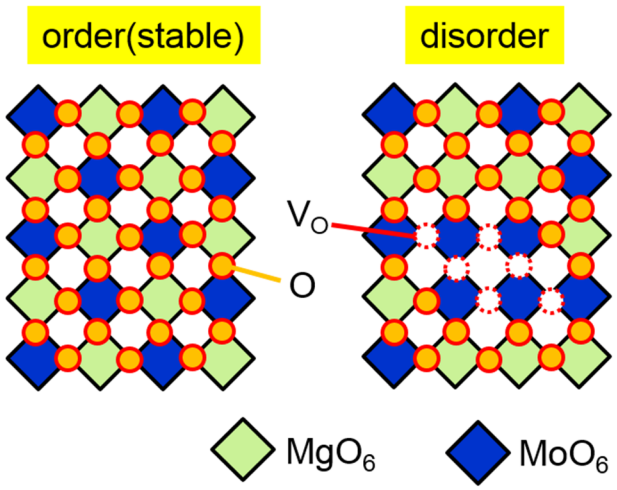

Figure 1-12. Simplified Sr_2MgMoO_6 structure and oxygen positions (orange circles) in it. Green and blue squares describes MgO_6 and MoO_6 octahedral, respectively. Note that blank circles of V_O in "disorder" picture are located at $Mo^{5+}–V_O^{\bullet\bullet}–Mo^{5+}$.

1.4 Purpose of this study

As mentioned above, transition-metal oxides with the double-perovskite structure $A_2BB'O_6$ exhibit a variety of electric properties depending on the combination of *B*- and *B*'-site cations, and their physical properties are sensitively correlated with the extend of ordering. Among those double perovskite compounds, SMM has attracted much attention as an anode in SOFCs. However, low conductivity of SMM does not meet the practical requirement. Here, introducing *B*-site disorder in SMM is expected to result in an increase of δ, though SMM belongs to "ordered perovskite" mainly due to the large difference in ionic valence between Mg^{2+} and Mo^{6+}.

In this study, I focused on PLD which has great potential to control *B*-site order of double perovskite in a wide range because of its non-equilibrium nature. I investigated thin films growth of SMM; effects of substrate temperature and oxygen partial pressure on the crystal structure of SMM including cell parameters and the extent of ordering. In addition, in order to characterize the oxygen-vacant SMM films, "bulk-sensitive" hard x-ray photoemission spectroscopy and resistivity measurements were conducted.

Chapter 2 Experimental method

2.1 Pulsed Laser Deposition

Pulsed laser deposition (PLD) [68] is a type of physical vapor deposition technique which uses focused pulsed laser beams for an ablation of solid source (called target). This technique is capable of vaporizing even high boiling-temperature ceramics. PLD enables stoichiometric transfer of atomic composition from source to samples if the growth condition is well optimized. In addition, the thickness of film is precisely controllable by tuning the number of laser pulses. Because of these advantages mentioned above, PLD have been employed to grow high-quality thin films of various materials including multi-component functional materials such as high-critical-temperature superconductor $YBa_2Cu_3O_{7-\delta}$ and superlattices with periodicity of nanometer scale [50, 51].

Principle

PLD growth consists of the following three processes. The first process is the ablation of target [52]. When focused pulsed laser beams with a high energy density (fluence) is absorbed on the surface of solid target, its electromagnetic energy is immediately converted to electronic excitation. In particular, the absorption efficiency is usually very high for ultraviolet pulsed-laser because of the generation of electron-hole

pairs in solids. The surplus energy on the excitation and the power from the successive laser are transported to thermal energy on the surface. Then, the surface region of target vaporizes when the temperature reaches above boiling point. .

The second process is the transport of ablated species to the substrate. During PLD experiment, one can observe a luminescent pillar, called as a plume, standing on the target surface. The plume contains ablated species including atoms/ions and their excited states or clusters. The plume consists of two distinct components, thermally evaporated part and non-thermally ablated part, and the fraction of the latter tends to increase with increasing the laser power because the ionic species can absorb the pulsed laser [53]. The non-thermal component in the plume is much forward-directed, stoichiometric (same composition with the target), and dominates thin-film growth. In addition, the species are

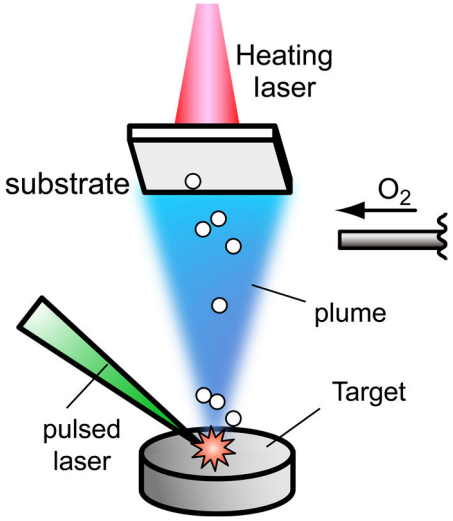

Figure 2-1. Schematic of fundamental PLD process.

accelerated and their kinetic energy reaches as high as a few-10^2 eV, which allows to grow thin films under non-equilibrium conditions.

The final process is the deposition. The ablated species reached on a substrate which is located at the top of the plume and crystallized on the substrate. The substrate works as a template for the thin film growth. Therefore the quality of the surface is very important to fabricate high quality films. For example, in case of perovskite $SrTiO_3$, which is one of the most frequently used as substrates for the fabrication of perovskite thin films, the way of surface etching by using buffered-HF solution had been established in order to obtain atomically flat surfaces [54].

Description of PLD experiment

The PLD target is a high-density sintered pellet composed of aiming material. In this study, the target was synthesized by solid state reaction of source compound powders, as follows. Stoichiometric amounts of source compounds are mixed well in a mortar. After pre-sintering for releasing carbon dioxide from metal carbonates and successive grinding, the mixed powder was pressed into a pellet and sintered in a furnace at high temperature.

Ultraviolet pulsed laser, the fourth harmonic of Nd:YAG laser (wavelength = 266 nm) or KrF excimer laser (wavelength = 248 nm) was employed for ablation. Infrared laser was absorbed by a graphite plate for heating the substrate. The substrate temperature was monitored with a pyrometer. The radiation factor of the graphite plate was set to 0.85.

The background pressure inside PLD chamber was kept in high vacuum (base pressure ~ 1×10^{-8} Torr) by combining rotary pump and turbo molecular pump. Such high vacuum could maintain a pure environment for the deposition and allow to conduct experiments with good reproducibility. High-purity oxygen gas was introduced through a variable leak valve for controlling the oxygen partial pressure during the deposition. Electron gun for reflection high energy electron diffraction (RHEED) was also equipped for *in-situ* monitoring of crystal growth.

Actual PLD procedures are described below:

1. Single crystal substrates were cut into pieces with 5 mm squares.
2. The substrates were washed in acetone and ethanol in an ultrasonic bath.
3. The substrates were fixed on a clean graphite plate with silver or platinum paste, which substantially improved heat conduction. Then the paste was thermally dried.
4. The substrates on the graphite plate and PLD target were introduced into a load- lock chamber of PLD apparatus.
5. The load-lock chamber was evacuated until high vacuum was achieved. Subsequently, the target and the substrates were transferred into the main chamber which equips with the components of UV pulsed laser, IR laser, variable leak valve, etc.
6. Substrate temperature, oxygen partial pressure, and pulsed laser power were adjusted.
7. To remove impurity particles on the surface of the target, short-time ablation was conducted after the substrates were shielded from the plume.
8. Deposition time and pulsed-laser frequency were set

9. Deposition was started.
10. After the deposition has finished, heating with IR laser and introduce of oxygen gas were stopped.
11. The samples were transferred to load-lock and taken out of the PLD chamber. Then, the samples were removed from the graphite plate. The paste backside the samples were erased.

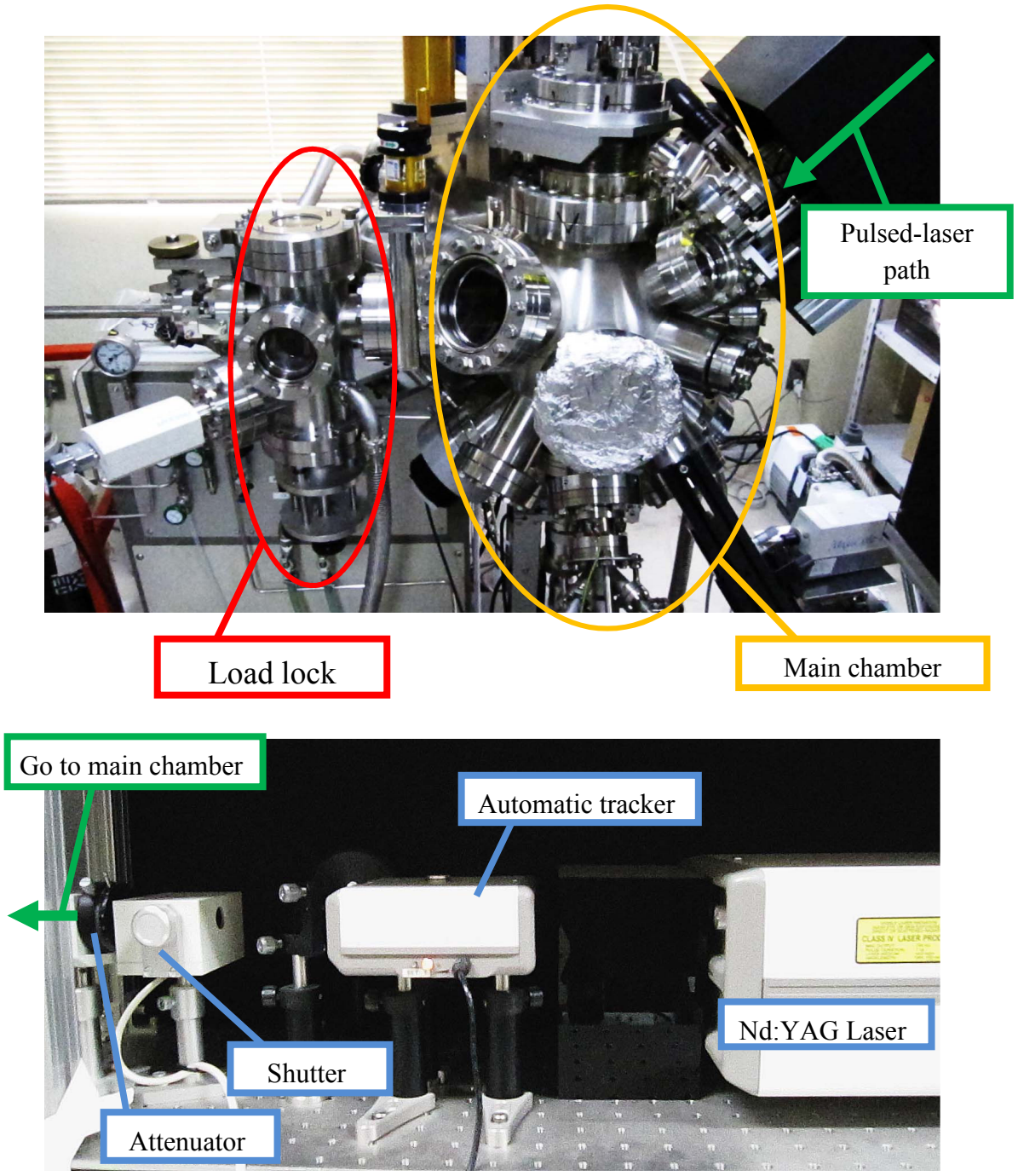

Figure 2-2. (Upper) Outlook of PLD chamber, L/L and main chamber (Bottom) Optical system of Nd:YAG pulsed-laser.

2.2 X-ray Diffractometry

X-rays are a part of electromagnetic waves whose wavelength are in the range of $10^{-1} - 10^{2}$ Å and are comparable to the length scale of the period of crystal lattice. Therefore x-rays are diffracted by crystal lattice working as a grating. X-ray diffractometry (XRD) is based on observation of intensity and diffraction angles of the elastically scattered x-ray by crystal lattice. The distance between the lattice plains d is determined as the Bragg's law:

$$2d \sin\theta = n\lambda,$$

where θ is the diffraction angle, n is an integer, and λ is the wavelength of x-ray. Therefore one can obtain detailed information about crystal structure, e.g.: in-plain and out-of-plain lattice constants of the thin-film samples.

Though the Bragg's law does not refer to the composition of atoms in crystal, the relative intensity of each diffraction peak is affected by the atomic composition in diffracting planes. The intensity of hkl peak (I_{hkl}) is given by

$$I_{hkl} = |F_{hkl}|^2 \times L \times p \times N \times D,$$
$$F_{hkl} = \Sigma_j \, (f_j \times \exp(-2\pi i(hu_j + kv_j + lw_j)) \, ,$$

where F_{hkl} is the structure factor, f_j is the atomic form factor, and u_j, v_j , w_j are the three-dimensional relative positions in the unit cell for atom j. The f value is basically proportional to the atomic number Z but tends to decay as increasing θ. Therefore, the following approximation formula is applied for the analysis of XRD intensity:

$$f(\theta) = \sum_{i=1}^{4} a_i \exp(-b_i(\frac{\sin\theta}{\lambda})^2) \ ,$$

where a_i and b_i are the empirical parameters. In this study, I adopted a_i and b_i (i = 1−4) from Table 6.1.1.4 in [55].

L, p, N, D are the Lorenz factor, the polarization factor, the absorption factor, and the Debye-Waller factor (temperature factor), respectively, and all of them are correction terms for actual x-ray diffraction intensities.

Lorentz factor calibrates deviation caused by the broadness of incident/diffracted x-rays. This factor has a different form depending on sample crystallinity, such as:

$L = 1 / (\sin^2\theta\cos\theta)$ for polycrystalline sample, or

$L = 1 / \sin 2\theta$ for single crystal sample

Polarization factor is a calibration term which considers the dependence of diffractive intensities relative to polarity of x-ray beam. Incident beam (characteristic x-ray of Cu Kα) contains any directions of polarization, and the x-ray whose electromagnetic wave is normal to the scattering plane only affects the diffraction. This factor is given by,

$p = (1+\cos2\theta)/2$, without monochromator, or

$p = (1+\cos2\theta_M \cos2\theta)/(1+\cos2\theta_M)$, with monochromator for the incident beam

where θ_M is the Bragg angle of monochromator. In this study, Ge (220) monochromator gives $2\theta_M$ of 45.3°.

Debye-Waller factor (temperature factor) considers the decrease of scattered x-ray caused by thermal oscillation of atoms. This factor is expressed as exp (-M), where M is proportional to $(\sin\theta/\lambda)^2$, and multiplied by the atomic form factor f.

Finally, absorption factor (from plain plate) is expressed as:

$$N = (2\mu)^{-1}\,(1 - \exp(-2\mu t / \sin\theta))\,.$$

where μ and t are the absorption coefficient and the thickness of sample, respectively. N can be regarded as a constant as $(2\mu)^{-1}$ if the sample is "thick" enough, i.e. $t \rightarrow \infty$. For typical oxides, "thick" indicates in the range of 10^0 -10^{-2} mm, which is clearly larger than typical thickness of PLD experiment. Therefore, it is obvious that the absorption factor significantly affects the diffraction intensities for thin film samples.

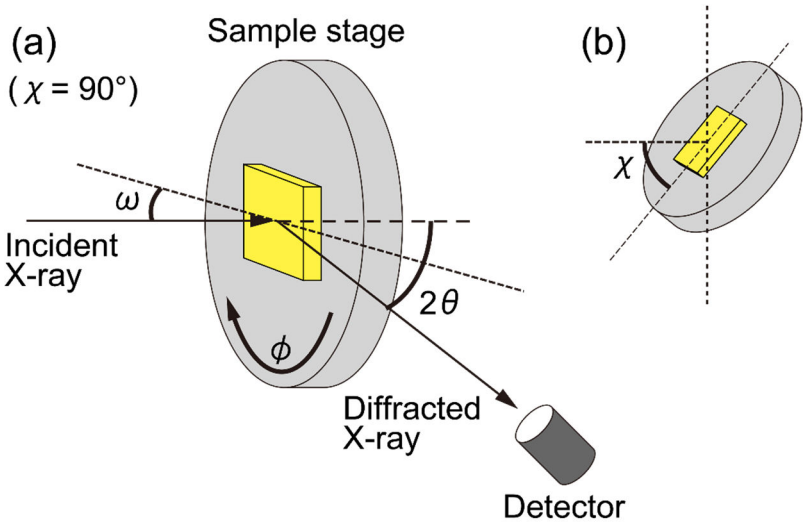

Figure 2-3. Schematic illustrations of XRD set up with noting four rotation angle, 2θ, ω, χ, and ϕ. (a) $\chi = 90°$ geometry for out-of-plane measurement. (b) $\chi < 90°$ geometry for in-plane measurement.

In this study, I used 4-axes XRD system (Bruker D8 discover). Characteristic x-ray emission from Cu Kα (λ = 1.5418 Å) was used as the incident x-ray beam. A Ge (220) monochromator was installed in the optical path when utilizing Cu $K\alpha_1$ (λ = 1.5406 Å) beam for high resolution measurements.

In this system, one can change the four rotation angles of 2θ, ω, χ, and ϕ, as illustrated in Fig 2-3. Here 2θ is the angle between the incident and diffraction beams, ω is the angle between the incident beam and sample plane, χ is the angle of rotation along of the film normal to the incident beam, ϕ is the angle of in-plane rotation.

I have measured out-of-plane ($\chi = 90°$) 2θ-θ XRD patterns in order to evaluate out-of-plane lattice constants and ordering ratio of *B* cations. I also performed in-plane ($\chi < 90°$) XRD measurements using a two-dimensional detector in order to evaluate the epitaxial strain of thin films from substrates.

2.3 Electric resistivity measurement

Electrical resistivity was measured by the four-probe method. The setup of this measurement is illustrated in Fig. 2-4. The two outer probes are used for flowing dc electric current (*I*) and the two inter probes are for measuring the voltage drop (ΔV). Resistivity (ρ) is evaluated by,

$$\rho = (\Delta V / I)\,(w \cdot t / L)\,,$$

where L and w are the size of the sample as defined in Fig. 2-4 and t is the thickness of the sample. In actual measurements, readouts of two voltmeters were averaged as ΔV to eliminate the influence of sample inhomogeneity. Furthermore, I measured ΔV twice with inverting the direction of dc current, in order to eliminate the influence of thermoelectric power at the contact between two different metals.

An advantage of the four-probe method is that extrinsic resistances can be neglected. The internal resistance of ammeter and the contact resistance at the current probes are both negligible when the applied current is small enough. The contact resistances at the voltage probes are also negligible because the voltmeter has so large inner resistance that the electric current hardly passes through the voltmeter. This measurement technique suits to samples with relatively small-resistivity such as metal or doped semiconductors.

In the actual measurements, I have performed using Physical Properties Measurement System manufactured by Quantum Design, Inc. This equipment can change the temperature in the range of 1.9 – 400 K. Indium metal or aluminum film was used as an electrode. Ohmic contact between the samples and these electrode metals were checked by two-probe I-V measurement by using the outer two probes.

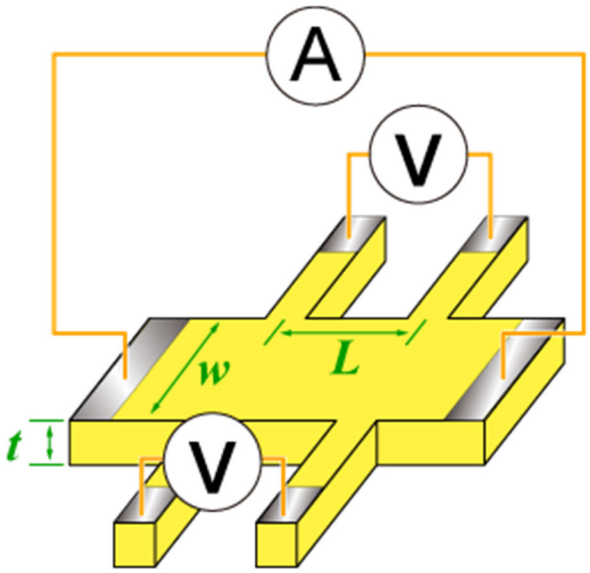

Figure 2-4. Schematic of four probe measurement. A and V stand for ammeter and voltmeter, respectively.

2.4 X-ray photoemission spectroscopy

Principle

X-ray photoemission spectroscopy (XPS) is a powerful technique to investigate electronic structures [56]. This technique is based on the observation of the number and kinetic energy of photoelectrons emitted from the samples when irradiated by x-ray. Figure 2-5 shows a schematic of XPS technique. The energy conservation in this photoemission process is represented by

$$(E_k)^{\text{vac}} = h\nu - \Phi - E_{\text{B}} ,$$

where $(E_k)^{\text{vac}}$ is the kinetic energy of photoelectron measured from the vacuum level $(E)^{\text{vac}}$,

$h\nu$ is the photon energy of x-ray, Φ is the work function of the solid, and E_B is the binding energy measured from the Fermi level (E_F). In practical experiments, since the sample surface and detector are set to be equipotential, the measured kinetic energy E_k of the emitted electron is referred to E_F. Then, one can obtain simple relationship,

$$E_k = h\nu - E_B.$$

According to the Koopmans' theorem [57], the value $-E_B$ can approximate the energy ε_k of the electron inside the samples, as long as both the initial and final states can be described as a N- and $(N-1)$-electron systems under Hatree-Fock approximation and the one-electron wave function remained unchanged during the removal of the electron. Therefore, the photoemission spectrum $I(E_B)$ is expressed as

$$I(E_B) \propto \Sigma_k \delta(E_B + \varepsilon_k) \propto N(-E_B).$$

Thus, as long as the one-electron approximation is valid, the intensity of measured photoemission spectrum was proportional to occupied density of states (DOS), $N(-E_B)$.

By using high energy of X-ray as a light source, one can detect electronic states in core levels. Those core level spectra are affected by chemical environment surrounding the targeting elements. Therefore, the binding energy of the core levels can be shifted depending on chemical-bonding states. This variation is called as chemical shifts which gives rich information about the chemical states of solids. For example, a cation with higher valence gives larger binding energy in photoemission spectra.

Probing depth

Photoemission spectroscopy is a surface-sensitive experimental technique because the mean free path of photoelectrons is as small as a nanoscale order. The escape

depth, which means how far an electron can travel through a solid without losing energy, is determined by electron-electron and electron-phonon interactions, and depends on the energy of photoelectron and a kind of element in solids. However, it is empirically studied that most elements show very similar kinetic-energy-dependence of inelastic path of electrons, as seen in Fig. 2-6 which summarize the data of inelastic mean free path from 41 kinds of simple metal [58].

In this study, XPS technique was used for the characterization of electronic states in SMM thin films with different amount of oxygen vacancy. As described in Chapter 4,

I employed two XPS setups: the laboratory XPS (PHI5000 VersaProbe, ULVAC-PHI) with photon source of Al Kα (1486.6 eV) combined with Ar ion gun for sputtering, and BL47XU with photon source from synchrotron radiation ($h\nu$ = 7.94 keV) with at the SPring-8 facility. In the latter measurement, spectra were collected by a Scienta R-4000 electron energy analyzer, with energy resolution of 0.3 eV. It is notable that the latter XPS measurement is more bulk-sensitive and the probing depth is ca. 10 nm. Detail description of the apparatus in BLX47XU is described in [59].

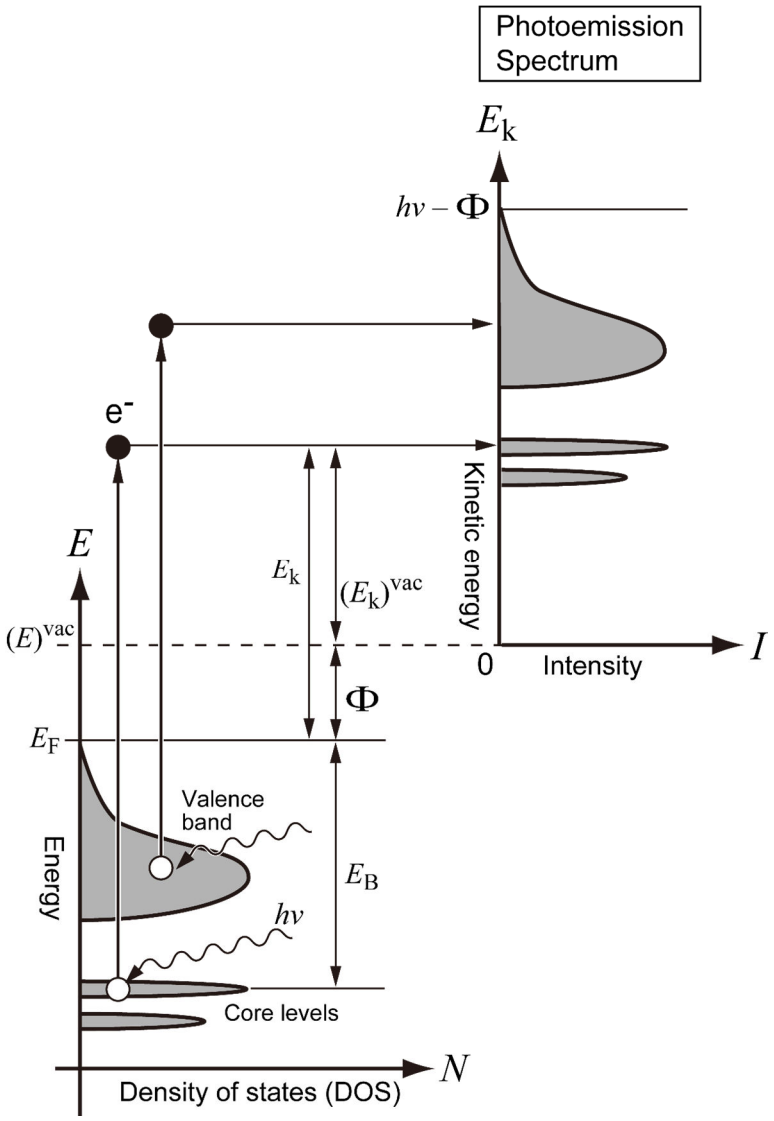

Figure 2-5. Schematic energy diagram of photoemission spectroscopy.

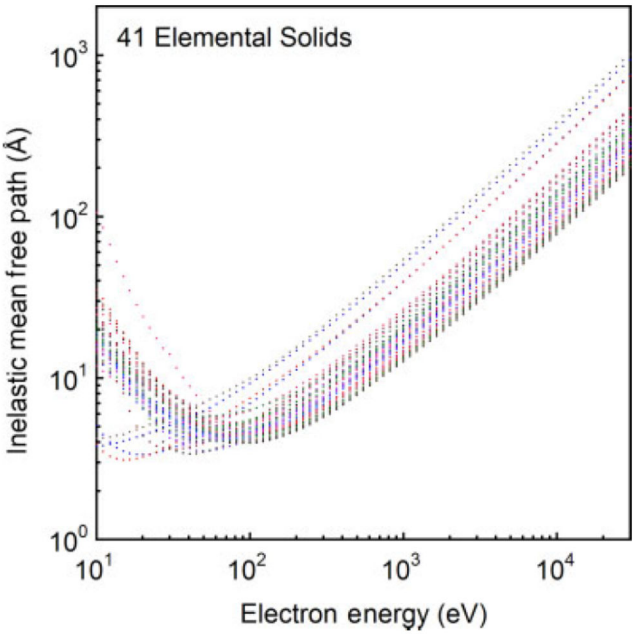

Figure 2-6. Calculated inelastic mean free path for 41 kinds of simple metals as a function of electron energy over the 50 eV− 30 keV range. [58] Copyright (c) 2011, John Wiley and Sons.

Chapter 3 Pulsed laser deposition growth of $Sr_2MgMoO_{6-\delta}$ thin films

3.1 Introduction

As mentioned in the introduction chapter, $Sr_2MgMoO_{6-\delta}$ (SMM) has attracted much attention as a promising anode material for hydrocarbon-fueled SOFCs, and introducing *B*-site disorder in SMM is expected to result in an increase of amount of oxygen vacancies. In this chapter, I describe epitaxial growth of SMM (111) thin films on $SrTiO_3$ (STO) (111) substrate by PLD. I have investigated dependence of lattice parameters, crystallinity, and *B*-site ordering ratio of the films on oxygen partial pressure (P_{O2}) and substrate temperature (T_s) during deposition. At the same time, I have prepared epitaxial SMM films with different extent of *B*-site ordering in a controlled manner. A series of SMM thin film samples with systematically different *B*-site ordering enable to investigate electric properties of SMM films.

3.2 Experimental procedure

A polycrystalline SMM pellet, used as the PLD target, was synthesized from mixed powders of $SrCO_3$, MgO, and MoO_3 (purity > 99.95%) by a solid-state reaction. It was pre-sintered at 800°C for 12 h and sintered at 1300°C for 24 h in air with intermediate grinding. SMM thin films were deposited on STO (111) and $GdScO_3$ (110) substrates by PLD technique. The substrate temperature (T_s) and oxygen partial pressure (P_{O2}) were varied as the main growth parameters. The fourth harmonic of a Nd:YAG laser (wavelength = 266 nm) or KrF excimer laser (wavelength = 248 nm) with energy density of 0.3 J/cm^2/shot and a repetition rate of 2 Hz was employed to ablate the target. The typical thickness of the films was ~50 nm. Crystal structures were characterized with XRD.

3.3 Results and discussion

Target preparation

Figure 3-1 shows an XRD pattern of the SMM target together with the result of simulation, indicating that the target was in single phase of double perovskite Sr_2MgMoO_6. The target had greenish white color, as reported previously [48]. When a unit cell of SMM is assumed to be a pseudo-cubic double perovskite, its lattice constant is calculated to be 7.886 Å, which is almost equivalent to the reported value, 7.888 Å. The density of the sintered SMM target was 2.37 g/cm^3 (45.8%), which was not very high

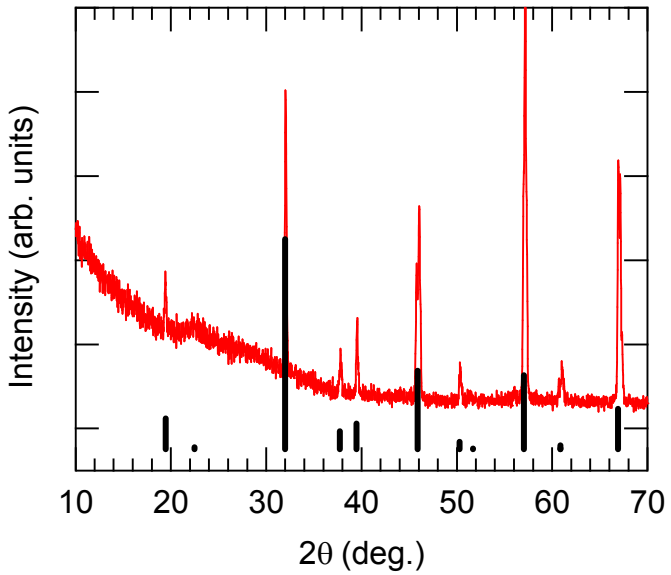

Figure 3-1. Powder XRD pattern from the SMM target: The red line is obtained data and the black bars are result of simulation.

as a PLD target. It is known that annealing at higher temperature (~1500°C) improves the density. However such a high temperature process results in partial decomposition to forming an impurity phase of $SrMoO_4$ [66]. Because the stoichiometry of target was more important in this study, such further sintering was not conducted.

PLD growth phase diagram and growth manner of SMM

Since a polycrystalline SMM target was obtained, I first constructed the PLD growth diagram of SMM thin films on STO (111), as shown in Fig. 3-2(a). In this diagram, three different phases were obtained: single-phase oxygen-vacant SMM ($\delta > 0$), oxidized SMM ($\delta = 0$) with secondary phase, and amorphous phase. Figure 3-2(b) shows typical

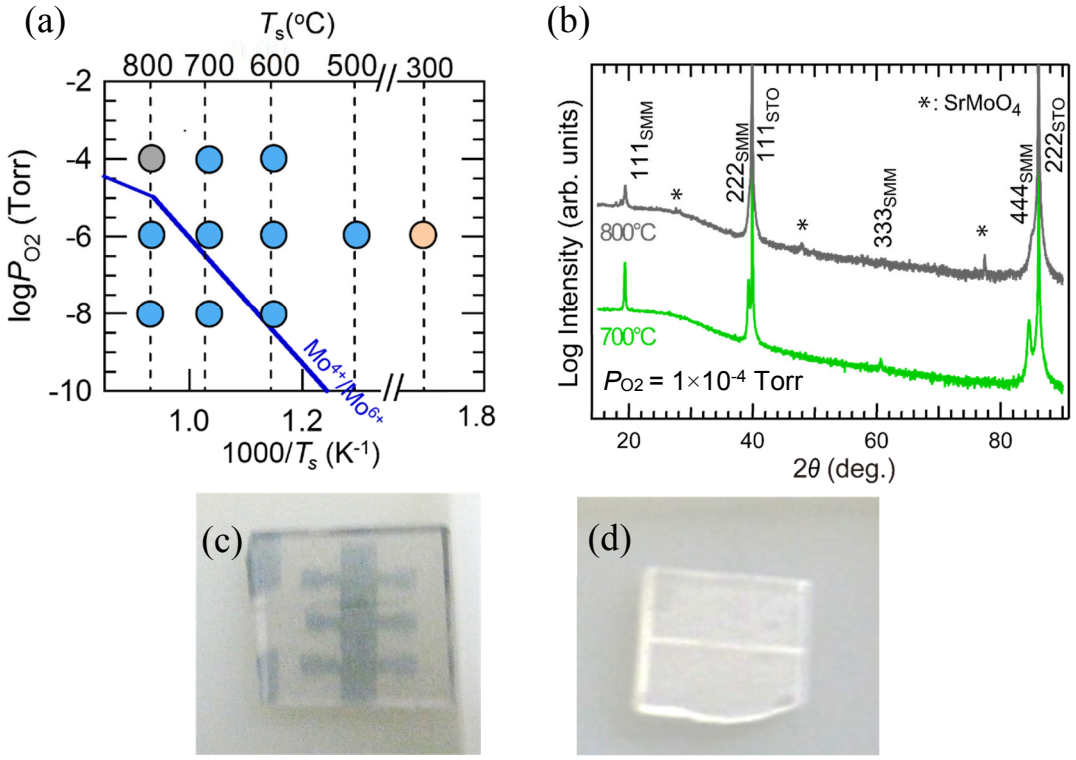

Figure 3-2. (a) Growth phase diagram of SMM thin films on STO (111) substrate as a function of oxygen partial pressure (P_{O2}) and substrate temperature (T_s) from SMM target. Blue, gray, and orange circles indicate single-phase oxygen-vacant SMM ($\delta > 0$), oxidized SMM ($\delta = 0$) with secondary phase, and amorphous phase, respectively. The thermodynamic boundary of Mo^{4+} (MoO_2) / Mo^{6+} (MoO_3) is also displayed with the blue line. (b) XRD patterns of SMM films deposited at (T_s, P_{O2}) = (800°C, 10^{-4} Torr) (gray) and (T_s , P_{O2}) = (700°C, 10^{-4} Torr) (green). (c) Photograph image of oxygen-vacant SMM film. (d) Photograph image of oxidized SMM film.

XRD 2*θ*-*θ* patterns from oxygen-vacant (green) and oxidized (gray) SMM. Both exhibit *hhh* diffraction peaks assignable to SMM and STO, indicating epitaxial growth of (111)-oriented SMM films on the STO substrates. In contrast, films in an amorphous phase showed no diffraction peak except for those of from the STO substrate. Figure 3-2(b) also reveals that the oxidized SMM contained a secondary phase of $SrMoO_4$, which

is commonly observed in the previous studies [48, 66]. On the other hand, no secondary phase, such as Mo, MgO or $SrMoO_4$, was observed in the oxygen-vacant SMM films. Figures 3-2(c) and (d) are photos of the oxygen-vacant and oxidized SMM films. The oxygen-vacant film has bluish color, apparently different from oxidized SMM film (transparent) or SMM target (greenish white).

From Fig.3-2(a), it is evident that oxygen-vacant SMM films can be obtained in wide P_{O2} range of $< 10^{-4}$ Torr. The figure also tells us that thermal equilibrium of Mo^{4+}/Mo^{6+} (data from [67]) does not govern the growth of SMM film unlike the case of thin-film Sr_2FeMoO_6 (see Fig. 1-4) or other double perovskites as mentioned in the introduction chapter.

I also performed in-plain XRD measurements. Figure 3-3 shows a typical two-dimensional 2θ-χ image around the STO 110 and SMM 220 diffraction peaks from (a) oxygen-vacant and (b) oxidized SMM film. As can be seen, the SMM 220 diffraction peak is located at the same χ position as the STO 110 peak at χ = 54.7º (arctan$\sqrt{2}$), indicating that the SMM films are free from lattice strain from the STO substrate,

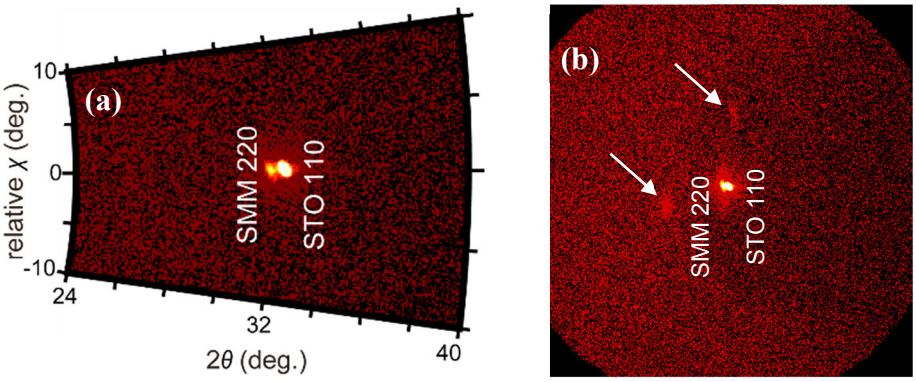

Figure 3-3. Two-dimensional XRD 2θ-χ patterns from (a) oxygen-vacant SMM, and (b) oxidized SMM around in-plane STO 110 diffraction. The white arrows in (b) denote diffraction peaks from $SrMoO_4$.

which is likely due to the large lattice mismatch at the interface. Figure 3-3(b) also exhibits $SrMoO_4$ impurity peaks indicated by white arrows. These peaks have a spot-like shape, indicating that $SrMoO_4$ is also grown in an epitaxial manner on STO (111).

Figure 3-4 shows *in-situ* reflection high energy electron diffraction (RHEED) results of oxygen-vacant SMM film (P_{O2} = 1×10^{-6} Torr, T_s = 700ºC). RHEED intensity sharply drops just after starting deposition, subsequently recovers, and gradually decreases; indicating three-dimensional growth mode of SMM. RHEED pattern from substrate showed spot-like patterns with Kikuchi lines which suggests good quality of the surface, as shown in Fig. 3-4(b). This Kikuchi lines instantly disappeared with the RHEED pattern being more spot-like shape just after starting deposition, as shown in Fig. 3-4(c). This pattern did not change until the deposition ended, as shown in Fig. 3-4(d).

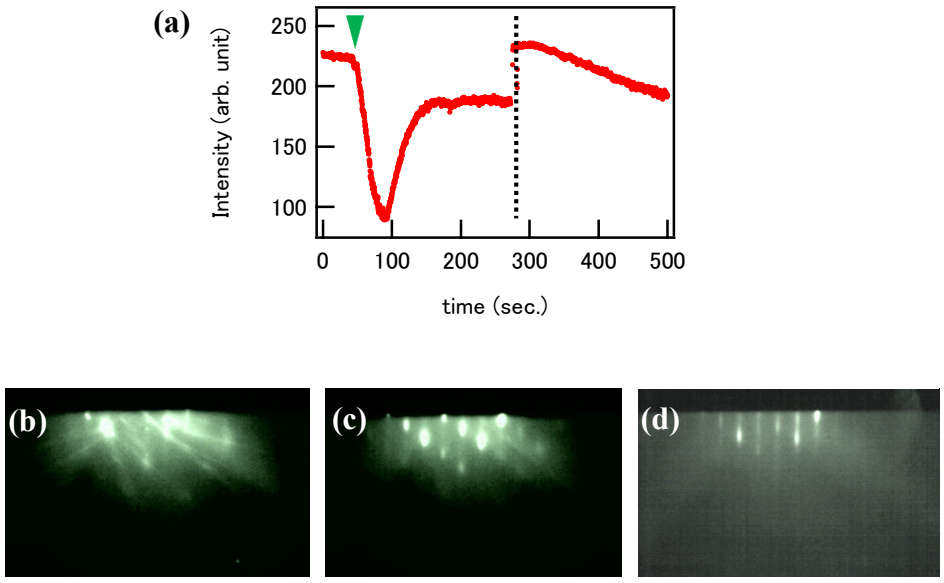

Figure 3-4. (a) RHEED intensity plot. The green arrow denotes the timing of start deposition. Intensity jump at time = 280 sec. is artificial, caused by tuning of detecting camera. (b)−(d) RHEED patterns from SMM/STO(111) film (b) before deposition (STO(111) substrate, time = 0) (c) at time = 90 sec. (d) after 90 minutes' deposition. Incidence direction of electron beam is [11$\bar{2}$]

Such a three-dimensional growth results in the presence of lateral facets and/or domain boundaries in SMM, which is preferable to increasing *B*-site disorder.

Oxygen partial pressure and substrate temperature dependence

Figure 3-5(a) shows 2θ-θ XRD patterns from the SMM/STO(111) films deposited under various P_{O2} at T_s = 700°C. All the samples exhibits *hhh* diffraction peaks from the SMM, indicating epitaxial growth of (111)-oriented SMM films on the STO substrates. Figure 3-5(b) shows the close-up view of Fig. 3-5(a) around SMM 444 diffraction, from which the shift of peak positions can be seen more clearly. The films fabricated under lower P_{O2} show SMM 444 peaks at lower 2θ, which implies that the crystal lattice of SMM films expanded when deposited more reductive deposition. The out-of-plane lattice constants (d_{111}) of these films calculated from the XRD data are plotted against P_{O2} in Fig. 3-5(c). There is a clear tendency that lattice constant increased as oxygen partial pressure during deposition decreased. Furthermore, these lattice constants are significantly larger than that of bulk samples. These results suggest that a considerable amount of oxygen vacancies were introduced in the SMM films fabricated by PLD.

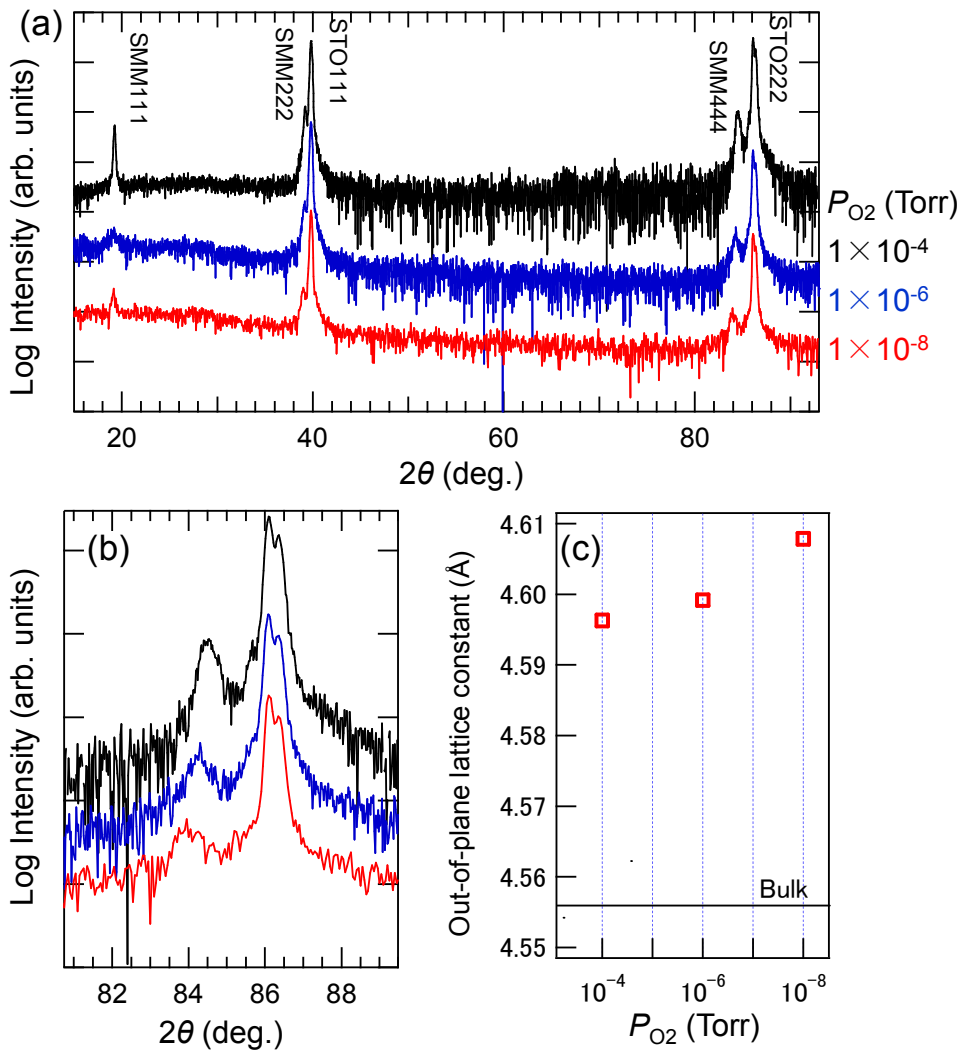

Figure 3-5. XRD 2θ-θ patterns from SMM films deposited under various P_{O2} at T_s= 700°C. (a) Wide scan view (covering SMM 111−444 peaks) (b) Close-up view around SMM 444 diffraction. (c) Out-of-plane lattice constant d_{111} vs. P_{O2} plot. The solid line in the graph indicates the value from bulk SMM (4.554 Å).

Figure 3-6(a) shows 2θ-θ XRD patterns of the SMM films deposited at 500–800°C for P_{O2} = 1×10^{-6} Torr. The four films in this figure also show (111)-oriented growth without any impurity phase. Unlike the P_{O2} dependence, however, peak position of SMM 444 is independent to T_s in this temperature region. This confirms that the SMM films contained significant amounts of oxygen vacancies.

Influence of T_s on the crystallinity of films was examined by XRD measurements. Figure 3-7 shows omega rocking curves around SMM 222 diffraction from the films fabricated at T_s = 600–800ºC. As T_s increased, the full-width of half-maximum (FWHM) decreased, indicating that the high temperature growth improved the quality of SMM films.

Based on the results of P_{O2} and T_s dependence on the crystallinity of SMM, three PLD conditions for obtaining oxygen-vacant SMM films and one condition for oxidized SMM were selected, as shown in Fig. 3-8(a), for further experiments. The deposition conditions of the four sample are following: Sample I was fabricated at (T_s, P_{O2}) = (800°C, 1×10^{-4} Torr); Sample II at (700°C, 1×10^{-4} Torr); Sample III at T_s = 700°C under a base pressure of ~1×10^{-8} Torr; and Sample IV at T_s = 800°C under the same base pressure. The Samples II–IV was single phase without any impurities from XRD patterns (Fig. 3-8(b)). The FWHM values of the SMM 222 rocking curves (Fig. 3-8(c)) were almost the same, 0.6°, for Samples II–IV proving that these samples have an equivalent crystallinity.

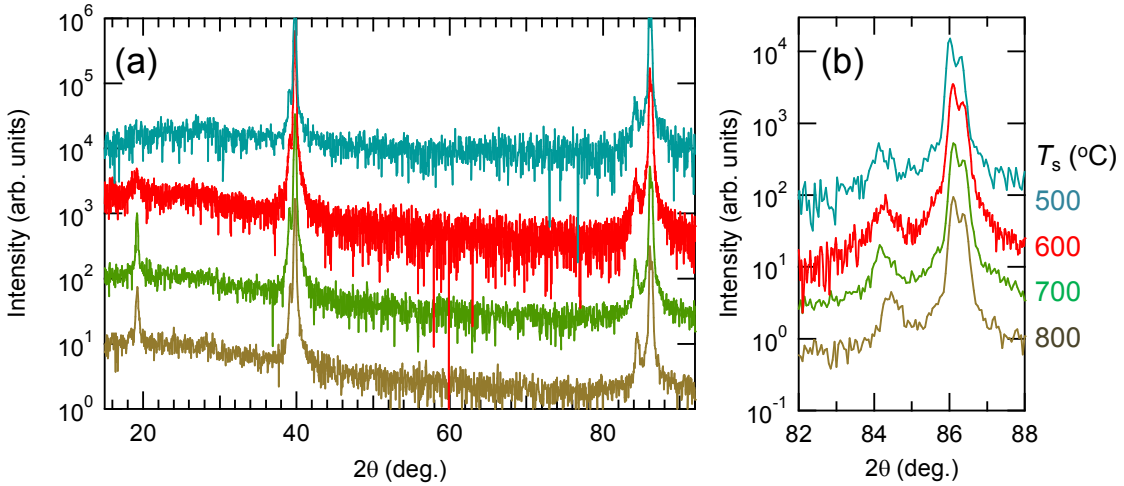

Figure 3-6. XRD 2θ-θ patterns from SMM films deposited at various T_s at $P_{O2} = 1\times10^{-6}$ Torr. (a) Wide view (covering SMM 111−444 peaks) (b) Close-up view around SMM 444 diffraction.

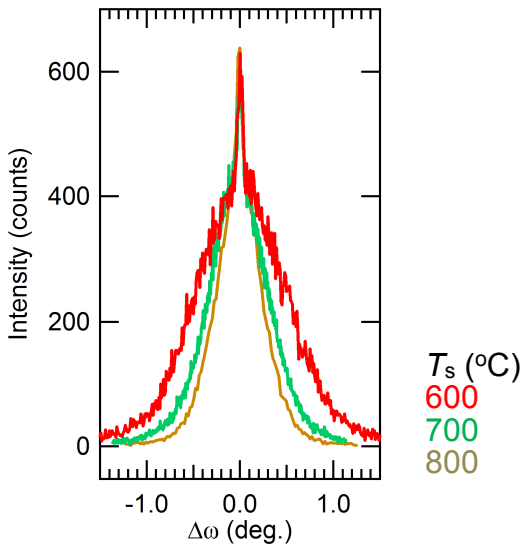

Figure 3-7. Omega rocking curves around SMM 222 diffractions from the SMM samples at T_s = 600–800ºC.

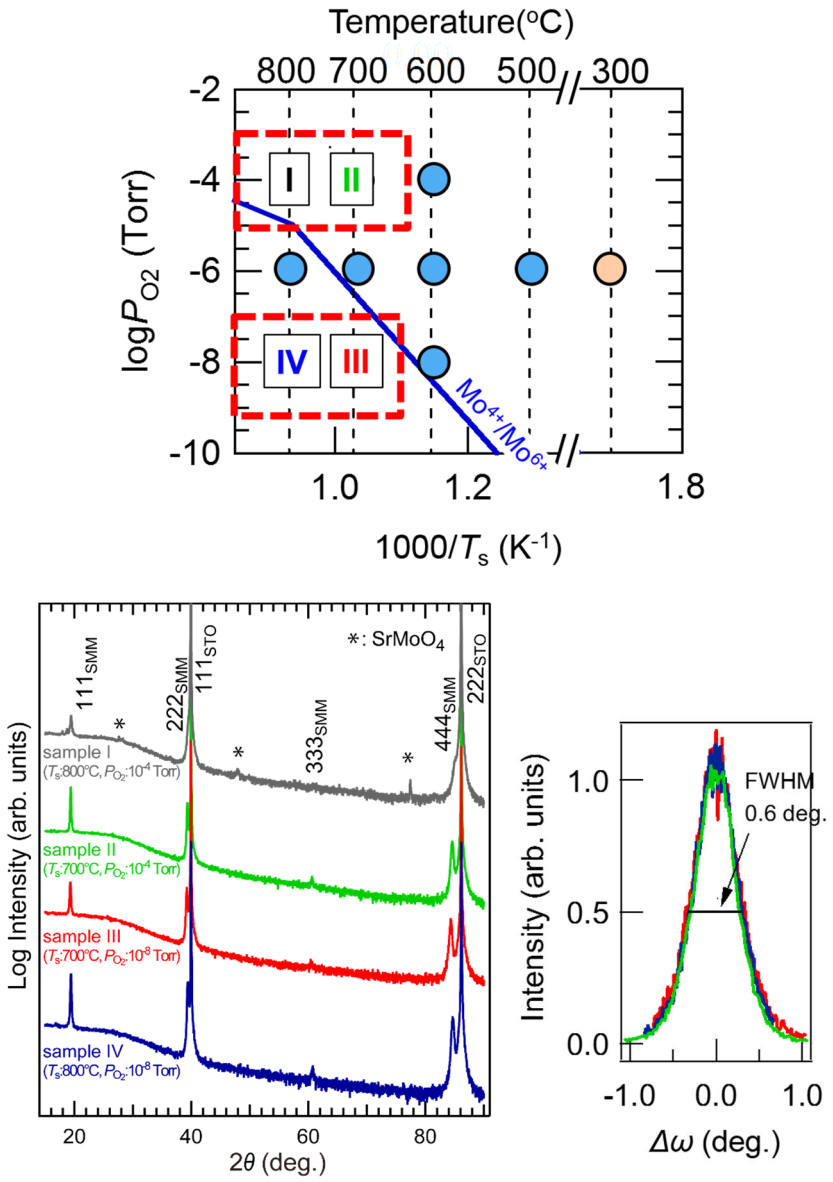

Figure 3-8. (a) Selected PLD conditions: Samples I−IV. (Phase diagram is the same as fig 3-2(a)). (b) XRD peak patterns of Samples I−IV. The data of Samples I and II are the same as in Fig. 3-2. (c) Rocking curves of SMM 222 peak from the samples II−IV.

Evaluating ordering ratio from XRD

In order to evaluate the ordering ratio of SMM films, I used the intensity ratio of the 111 superstructure peak to the 222 fundamental peak. Figure 3-9 shows schematic illustration of atomic arrangements of SMM films on STO (111) substrates. Perovsktie ABO_3 structure can be regarded as an alternate stack of AO_3 and B layers. Therefore, when double perovskite Sr_2MgMoO_6 is completely B-site ordered, its fundamental periodic structure is the four layers of "…-(SrO_3)-Mg-(SrO_3)-Mo-…", whereas the periodic structure is as short as two layers, "…-(Mg/Mo)-(SrO_3)-…, " in B-site random phase. This difference will cause the presence or absence of *hhh* diffractions with *h* being odd numbers. For more quantitative analysis, the diffractive intensity of 111 and 222 were calculated based on the structural factor F_{hkl} of perovskite as follows:

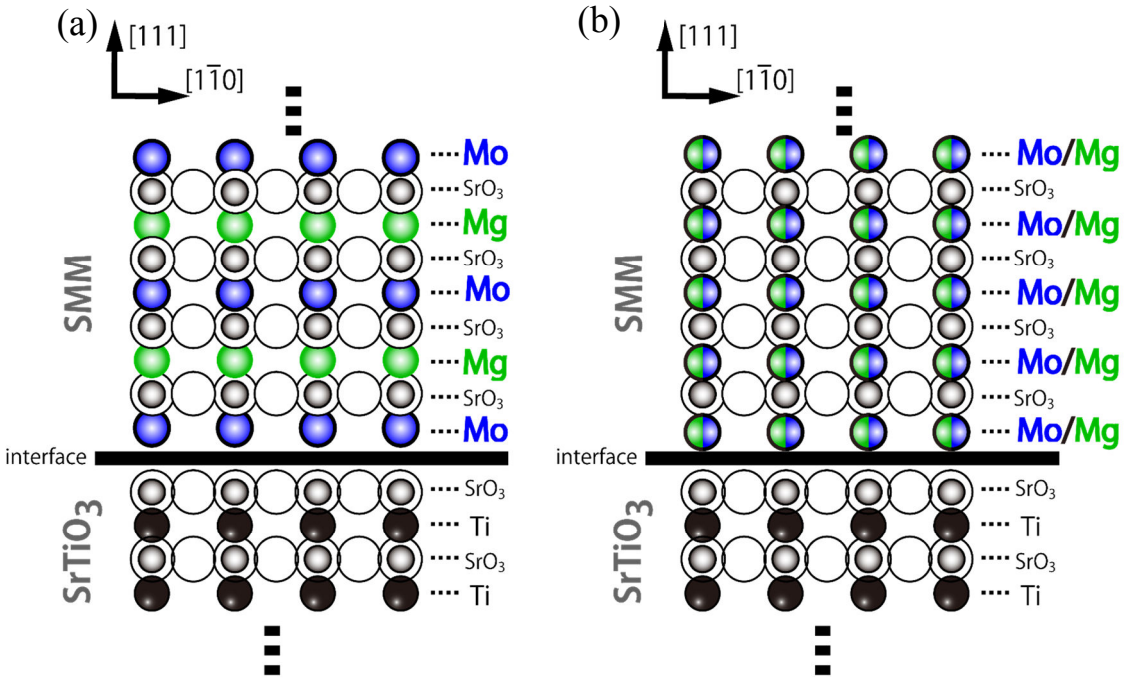

Fig. 3-9. Schematic illustration of atomic arrangements of SMM films on STO (111) substrates. (a) Perfectly B-site ordered states. (b) B-site random state.

Table 3-1. Atomic scattering factors of O, Sr, Mo, Mg for SMM 111 and 222 diffraction peaks; $2\theta = 19.4$ and 39.4 correspond to 111 and 222 diffractions.

Element	Atomic scattering factor	
	For 111 peak ($2\theta = 19.4°$)	For 222 peak ($2\theta = 39.4°$)
O	7.11	5.31
Sr	34.0	29.2
Mo	38.2	32.2
Mg	10.3	8.48

Table 3-2. Lorentz factor, polarization factor, absorption factor, and Debye-Waller factor for SMM 111 and 222.

Parameter	For 111 peak ($2\theta = 19.4°$)	For 222 peak ($2\theta = 39.4°$)
L	17.6	4.40
P	0.977	0.906
N (when thickness = 50 nm)	9.63×10^{-4}	4.83×10^{-4}
D	0.988	0.953

$$F_{111} = R \times (f_{Mo} - f_{Mg})$$
$$F_{222} = f_{Mo} + f_{Mg} - 2f_{Sr} - 6f_{O}$$

Here the f_M is the atomic factor of each atoms and deviation caused by atomic displacements are neglected [25]. The atomic factor of O, Mg, Sr, and Mo can be calculated from

$$f(\theta) = \sum_{i=1}^{4} a_i \exp(-b_i(\frac{\sin\theta}{\lambda})^2),$$

with adopting coefficient a_i and b_i (i = 1−4) from Table 6.1.1.4 in reference [55]. The f values for individual elements are summarized in Table 3-1. In addition, the correction terms, which are also θ dependent, were calculated as shown Table 3-2. Then, R was evaluated with the formula, $I_{111} / I_{222} = 2.83R^2$, for 50-nm-thick SMM film.

Figure 3-10(a) shows XRD 2θ-θ pattern from Samples II−IV. The diffraction peak of SMM 111 and 222 were well fitted by single Gaussian function. Background for SMM 222 originating from the shoulder of STO 111 peak was subtracted by fitting curve of the STO peak with Lorentzian function. The resulting I_{111} / I_{222} values for Samples II, III, and IV were 1.33, 1.21, and 1.13, respectively. Using this value, the Mg/Mo ordering ratio was estimated to be 69%, 65% and 63% for Samples II, III, and

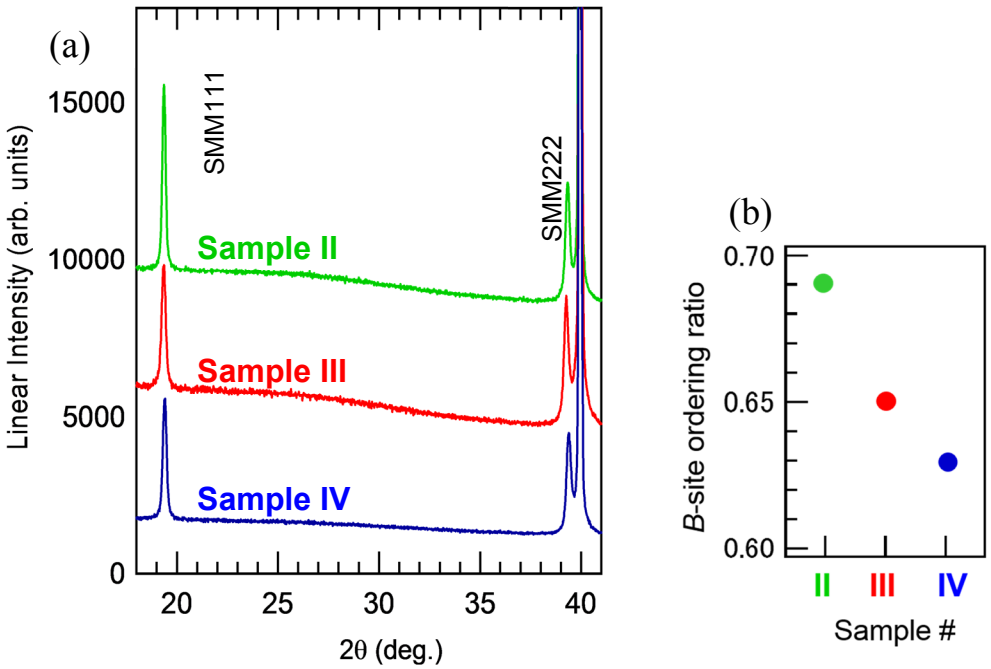

Fig. 3-10. (a) XRD 2θ-θ pattern from Samples II−IV in the range including SMM 111 and 222 diffraction. (b) B-site ordering ratio vs. Sample # evaluated from intensity ratio of 111 to 222.

IV, respectively. Notably, these ordering ratio of SMM films I manufactured were much lower than that for polycrystalline samples. In addition, considering the tendency that the amount of oxygen vacancy increases with decreasing the *B*-site ordering in polycrystalline SMM, the amount of oxygen vacancy decreased most in Sample IV, less in Sample III, and the least in Sample II. These results indicate that I have successfully fabricated SMM films with same crystallinity and different extent of *B*-site ordering in a controlled manner.

Substrate dependence

Finally I briefly describe results of SMM thin films on $GdScO_3$ (110) substrate. $SrMoO_3$ (cubic, a = 3.975 Å) is also perovskite molybdate and has similar lattice constant to SMM ($a/2$ = 3.944 Å for δ = 0). In previous studies, $SrMoO_3$ on $GdScO_3$ (110) showed better crystallinity (FWHM of rocking curve = 0.045°) [70] compared to that on STO (001) (FWHM of rocking curve = 0.259°) [71], because lattice matching was better for $GdScO_3$ (pseudocubic a ~ 3.96 Å) than STO (a = 3.905 Å). This affected the resistivity of films: ρ(300 K) = 117 $\mu\Omega$ cm on STO and 29 $\mu\Omega$ cm on $GdScO_3$. Therefore it is expected that film-quality of SMM is improved by using $GdScO_3$ substrate.

SMM on $GdScO_3$ (110) was fabricated on the same condition as Sample III. Figure 3-11 shows XRD results for the film. The out-of-plain 2θ-θ wide scan (Fig. 3-11(a)) shows $GdScO_3$ *hh*0 peaks without any impurity peak. The high resolution 2θ-θ scan around $GdScO_3$ 220 peak shows a clear peak with Laue-fringes from SMM films (Fig. 3-11(b)). Omega rocking curve scan for this SMM peak exhibits a very sharp peak whose FWHM is as small as 0.05° (Fig. 3-11(c)), which is much lower than that on STO.

These indicate high crystallinity of the SMM film. In addition, two-dimensional 2θ-χ image around the $GdScO_3$ 224 diffraction peaks (Fig. 3-11(d)). A spot-like diffraction peak from SMM which is located at close to the $GdScO_3$ 224 peak is observed. The lattice constant is calculated to be c = 4.019 Å and a ~ 3.95 Å, suggesting coherent growth of SMM on $GdScO_3$ unlike on STO.

Though the SMM film on $GdScO_3$ showed good crystallinity, it was difficult to discuss *B*-site ordering ratio because superstructure SMM 111 peaks were overlapped with $GdScO_3$ peaks. High intensity XRD such as synchrotron radiation x-ray or direct observation of crystal structure in atomic-scale such as transmission electron microscopy may provide useful information about *B*-site ordering.

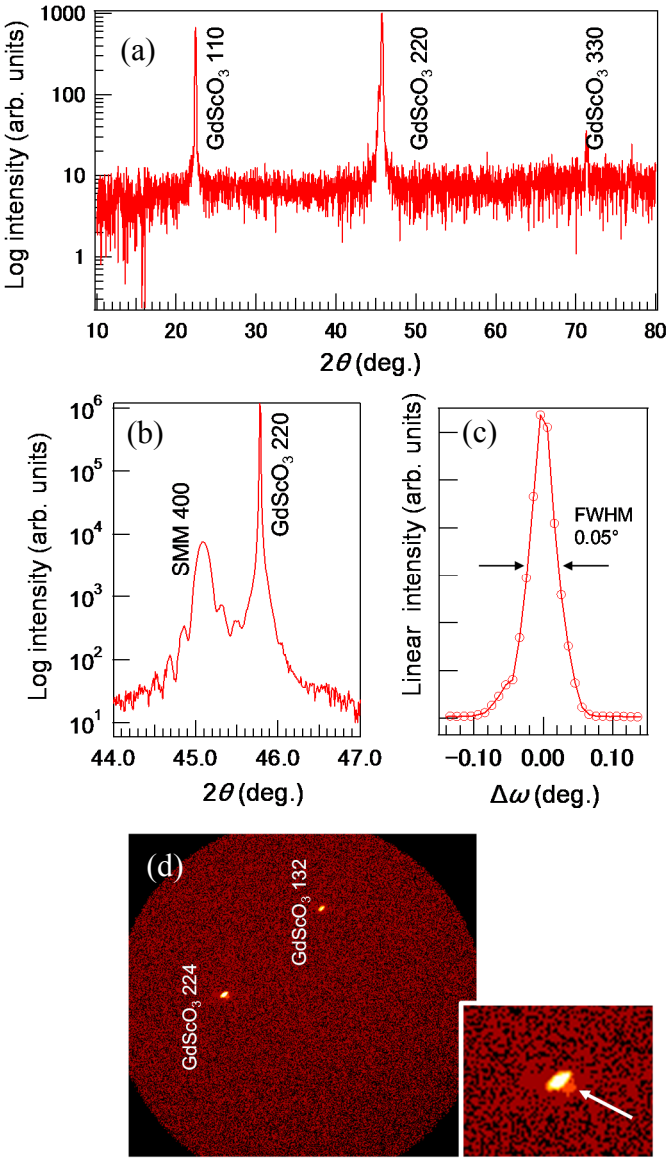

Figure 3-11. XRD results from SMM/$GdScO_3$ (110) (a) out-of-plain 2θ-θ wide scan. (b) High resolution 2θ-θ scan. (c) Omega rocking curve for SMM 400 peak. (d) two-dimensional 2θ-χ image; wide scan (left) and close-up around $GdScO_3$ 224 diffraction (right). The white arrow denotes a diffraction peak from SMM.

3.4 Summary

I have studied epitaxial growth of SMM thin films on STO (111) substrate. As a result, I successfully fabricated epitaxial thin films of oxygen-vacant and oxidized SMM. The lattice constant, crystallinity, and *B*-site ordering ratio of oxygen-vacant SMM thin films depended on the substrate temperature and oxygen partial pressure during PLD growth. RHEED result suggested three-dimensional growth, which would result in rough surfaces of SMM. The oxygen-vacant SMM films showed larger lattice constants compared to polycrystalline samples. The extent of *B*-site ordering decreased down to 63% which was much smaller than those for bulk samples. A series of SMM samples with the same crystallinity and systematically varied *B*-site ordering enabled to investigate the electronic states and electric properties of SMM films

Chapter 4 Electronic structure and electric properties of $Sr_2MgMoO_{6-\delta}$ thin films

4.1 Introduction

In this chapter, I present characterization of the electronic states and electric properties of the SMM epitaxial thin films prepared in the previous chapter. XPS measurement of a series of SMM films with different *B*-site ordering revealed the relationship among the extent to *B*-site ordering, oxygen-vacancy δ, and resistivity of SMM. Notably, it was found that the SMM films fabricated by PLD contained a sizable amount of oxygen vacancies and exhibited remarkably low resistivity compared to polycrystalline SMM reported previously.

4.2 Experimental procedure

I selected the four SMM thin-film samples, Sample I−IV shown in Fig. 4-1, from thin films for characterization. Note that these four samples have the equivalent

---

A part of this chapter (including Figs. 4-6, 4-7(a) and 4-9(a)) has been published in Applied Physics Letters. Reprint with permissions from "Sr_2MgMoO_6 thin films fabricated using pulsed-laser deposition with high concentrations of oxygen vacancies," K. Shigematsu, A. Chikamatsu, T. Fukumura, S. Toyoda, E. Ikenaga, and T. Hasegawa, Appl. Phys. Lett. 104, 261901 (2014)."

crystallinity with different extents of *B*-site disorder, which allow to discuss correlation of ordering and oxygen-vacancies clearly. XPS technique was used for the characterization of electronic states in SMM thin films with different amount of oxygen vacancy. I employed two XPS setups: laboratory XPS (PHI5000 VersaProbe, ULVAC-PHI) with photon source of Al Kα (1486.6 eV), and HAXPES with photon source from synchrotron radiation ($h\nu$ = 7.94 keV) in BL47XU with at the SPring-8 facility. The former XPS measurement was combined with Ar ion gun for sputtering. In the latter measurement, spectra were collected by a Scienta R-4000 electron energy analyzer, with energy resolution of 0.3 eV. DC resistivity was measured by the four-probe method using Physical Properties Measurement System, Quantum Design, Inc. The temperature dependence of resistivity was measured in the range of 10–300 K.

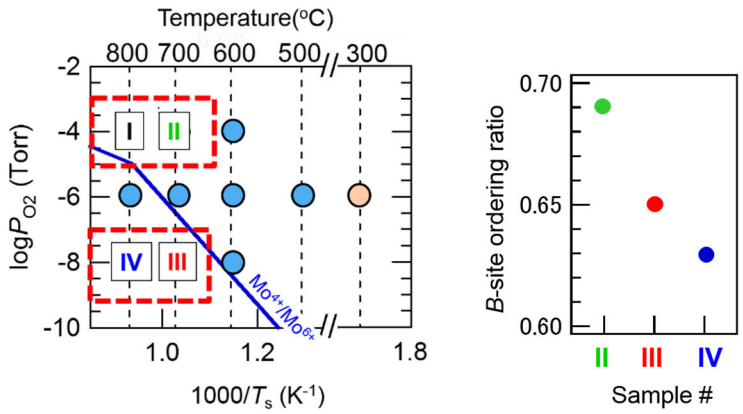

Figure 4-1. (a) PLD conditions of SMM Sample I–IV. (Figure same as Fig 3-8(a)). (b) The variation of *B*-ordering ratio as a function of Sample number (Figure same as Fig. 3-10(b)).

4.3 Results and discussion

At first, I would like to explain how tricky XPS measurements of molybdenum compounds are. It is well known that near the surface of molybdenum compounds is easily oxidized. For example, as mentioned in the introduction chapter, surfaces of polycrystalline Sr_2FeMoO_6 are covered with oxidized insulating layers, which could work as barriers for tunneling magnetoresistance [6]. Such oxidized layers prevent the XPS detection of bulk electronic states due to its short probing depth. Figure 4-2 shows Mo 3*d* XPS spectra from $SrMoO_3$ thin film studied previously [60]. When hard x-ray was used as a light source, the resultant spectrum was dominated by two structures that were very similar to MoO_2 (Mo^{4+}). Whereas, when soft x-ray was used as a light source, different two structures evolved, whose location were almost the same as those of MoO_3 (Mo^{6+}). These results indicate that soft x-ray cannot detect the bulk states of $SrMoO_3$ films covered with surface oxidized layers. To solve this problem, here I employed two approaches: (1) removing oxidized topmost layers by *in-situ* sputtering during XPS, and (2) using hard x-ray as a light source.

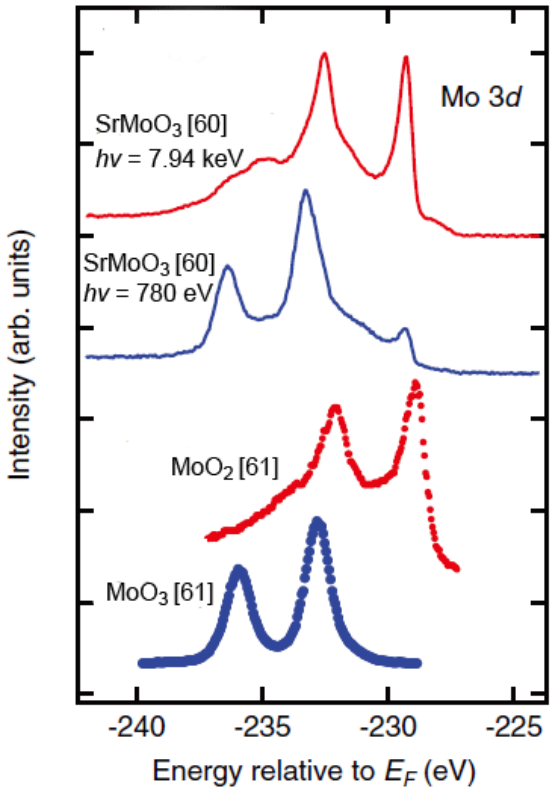

Figure 4-2. The Mo 3*d* spectra of $SrMoO_3$ thin film by both hard x-ray (solid red line) and soft x-ray (solid blue line), plotted together with the reference spectra of MoO_2 (red dots) and MoO_3 (blue dots). [60, 61]. Reprinted figure with permission from [60]. Copyright 2014 by the American Physical Society.

XPS measurement with Ar sputtering

At first, I describe the results of XPS spectroscopy of Sample III using Al Kα generation combined with Ar sputtering. Fig. 4-3 (a) shows a XPS survey spectrum. The peaks from constituent ions of SMM and C 1*s* originating from surface contamination is observed. Figure 4-2(b) is sputtering-time evolution of Mo 3*d* region. Before sputtering, oxygen-vacant SMM film exhibited primarily the strong Mo^{6+} features. Then, Ar beam at an ion-beam energy of 500 eV was irradiated, erasing the carbon on the surface completely without sputtering SMM. However, Mo^{6+} also decreased without saturating as the sputtering time increased. Then, I applied subsequent Ar beam irradiation at an ion-beam energy of 2 keV, which is necessary for sputtering SMM film. As a result, it is observed that only the 30 s sputter changed into metallic Mo^0, which is not consistent

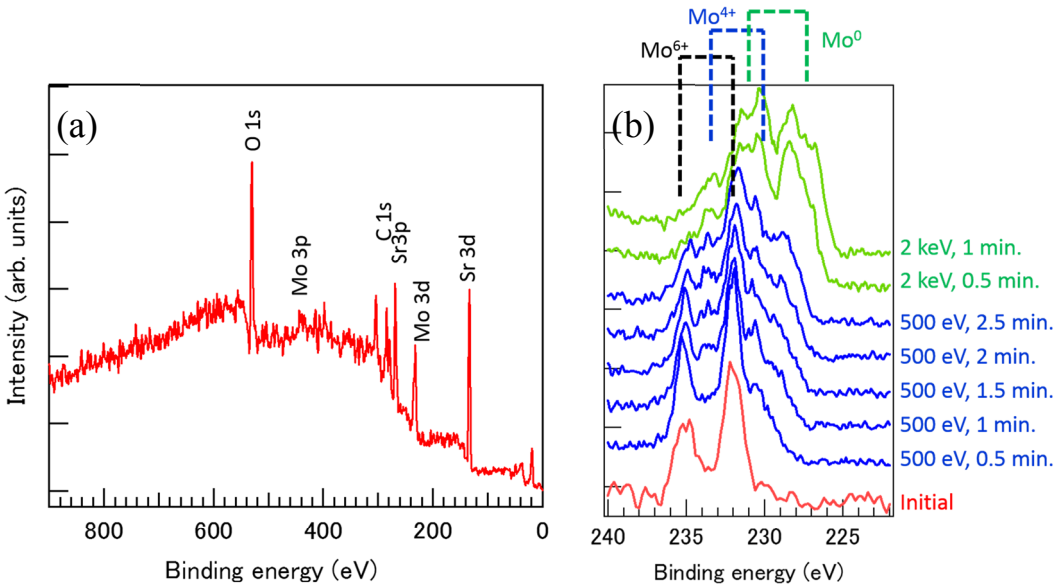

Figure 4-3. XPS of Sample III with Al Kα source: (a) Survey spectrum and (b) sputtering-time evolution of Mo 3*d* spectra. Peak positions of Mo^{6+}, Mo^{4+} and Mo^0 are also shown.

with XRD results showing single-phase SMM pattern. It is more reasonable that higher oxidation state of molybdenum were reduced due to Ar exposure and finally changed to metallic Mo, as is also indicated in XPS study about Sr_2FeMoO_6 [62]. This causes a great uncertainty on the analysis of molybdenum state in oxygen-vacant SMM. Therefore, I concluded that the Ar sputtering technique is not applicable for the evaluation of oxygen-vacant SMM.

Hard x-ray photoemission core-level spectra

Next, I describe the results of HAXPES spectroscopy of SMM thin films. Figure 4-4 shows survey spectra from Samples II–IV. The peaks from constituent ions of SMM are observed, and no apparent differences are observed. A pronounced difference from

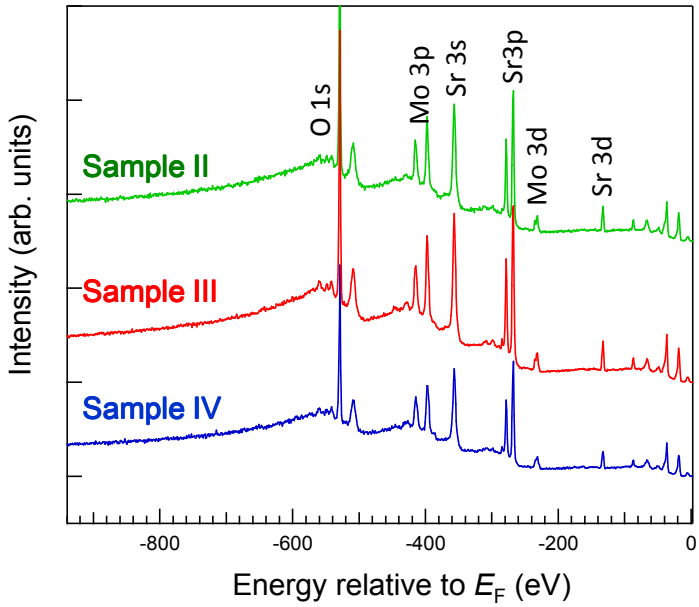

Figure 4-4. HAXPES survey spectra from Sample II–IV.

Fig. 4-3(a) can be seen in intensity of C 1*s* peak; the weaker strength in Fig. 4-4 represents high bulk-sensitivity in this HAXPES measurement.

Then, finer core-level spectra in Sr 3*d*, Mg 2*p*, O 1*s* and Mo 3*d* region are shown in Fig. 4-5. The Sr 3*d* spectra show two peaks composed of $3d_{5/2}$ and $3d_{3/2}$ peak which is typical specific to Sr^{2+} state. The Mg 2*p* spectra show typical specific to Mg^{2+} state. These two core-level spectra do not vary among Samples II−IV, suggesting that the valence states of Sr and Mg are sample-independent. O 1*s* spectra show a prominent single peak with a very small shoulder at the high binding-energy (left) side, suggesting that the SMM films are free from surface degradation and represent the bulk electronic properties.

The Mo 3*d* spectra show two prominent structures located at −233.3 and −236.5 eV corresponding to $3d_{5/2}$ and $3d_{3/2}$ of Mo^{6+} states in Sr_2MgMoO_6. In addition, a small peak between −233.3 and −236.5 eV, and shoulder peaks at low binding-energy side are recognizable, suggesting reduced fractions of molybdenum, Mo^{5+} and Mo^{4+}, were present. The intensity of these reduced fractions varied between different samples, in contrast to the Sr 3*d* and Mg 2*p* spectra. These results prove that only the valence state of Mo changed as a consequence of introduced oxygen vacancy in SMM. Here I would note that Mo^0 fraction (~ 228 eV for $3d_{5/2}$ peak) did not emerge in any samples, which suggests that the present SMM samples did not contain metallic Mo as I mentioned in the previous subsection.

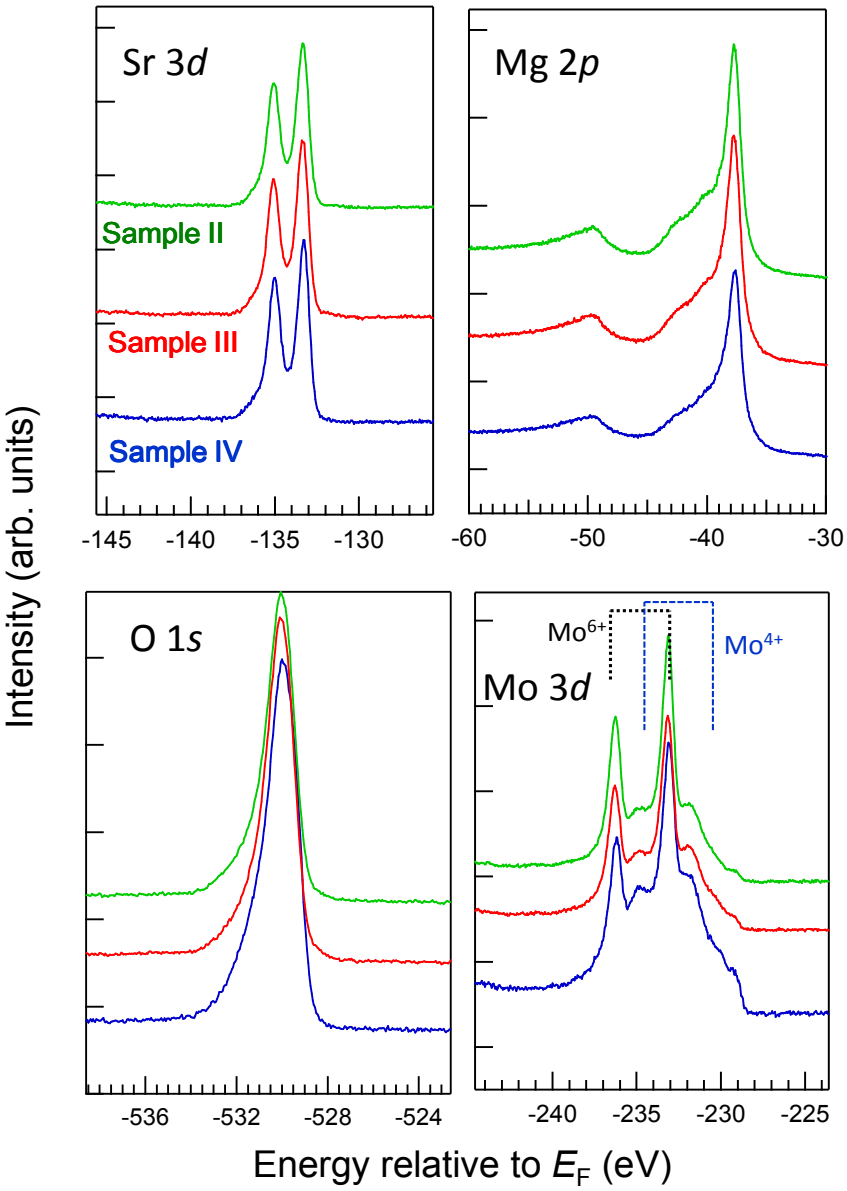

Figure 4-5. HAXPES core-level spectra of Sr 3*d*, Mg 2*p*, O 1*s* and Mo 3*d* from Samples II−IV.

Next, I attempted quantitative analysis of Mo 3*d* spectra. Figures 4-6(a)–(d) depict the Mo 3*d* spectra and their least-square fitting for Samples I–IV. Note that sample I was calibrated by fixing the peak position of Mo^{6+} $3d_{5/2}$ to 233.4 eV to eliminate the influence of charge-up. The Mo 3*d* spectra were reproduced well by combining the $3d_{5/2}$ ($3d_{3/2}$) components of Mo^{6+}, Mo^{5+}, and Mo^{4+}, corresponding to the peaks located at binding energies (E_b) 233.3(236.5), 232.0(235.0), and 230.4(234.1) eV, respectively, being consistent with [62]. The fractions of individual Mo components, $f(Mo^{6+})$, $f(Mo^{5+})$, and $f(Mo^{4+})$, calculated from the peak area intensities are presented for comparison in Fig. 4-6(e). The Mo^{6+}-component fraction tends to decrease in succession from Samples I to IV, whereas those of Mo^{5+} and Mo^{4+} increase. This suggests that δ increases in this order, which is consistent with the above argument regarding I_{111} / I_{222} in chapter 3. Assuming that Mo^{6+} is reduced to Mo^{5+} and Mo^{4+} by the formation of oxygen vacancies, δ can be deduced by using the relation $\delta = f(Mo^{5+})/2 + f(Mo^{4+})$. The calculated δ values are 0.22, 0.28, and 0.37 for Samples II, III, and IV, which are indeed much larger than the maximum δ in bulk, 0.046.

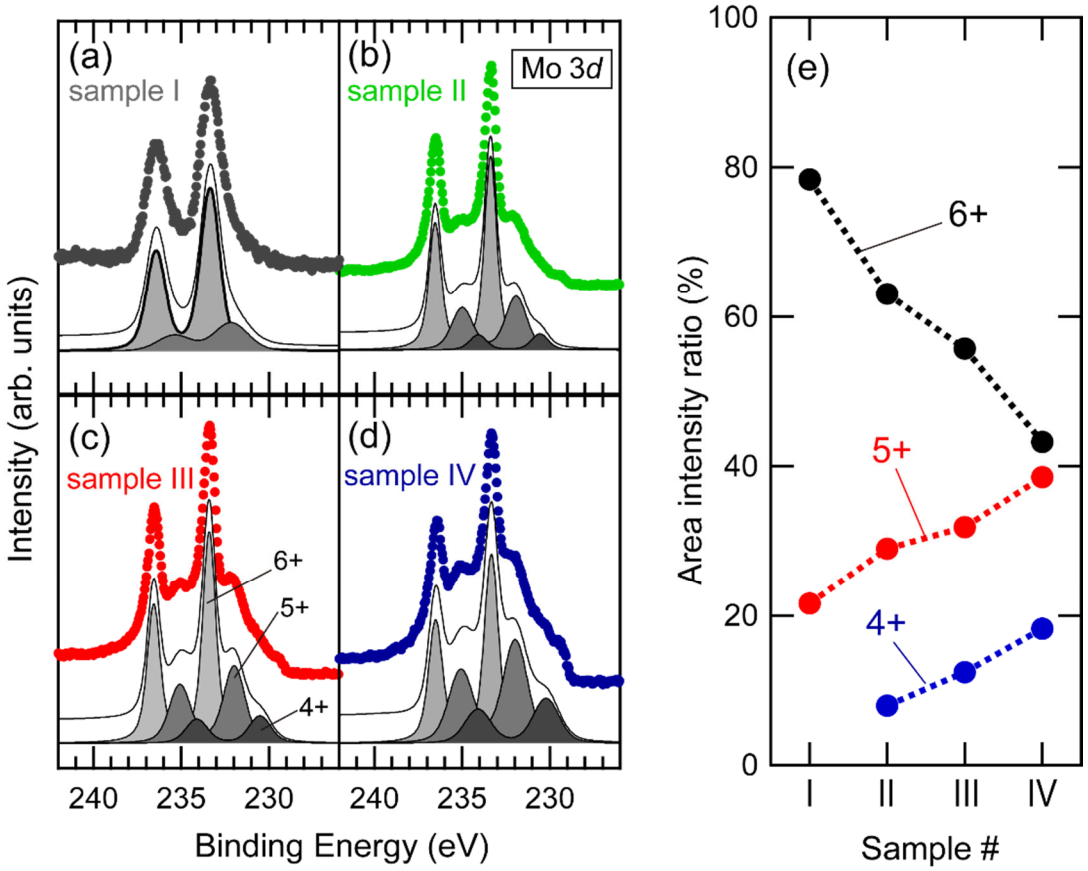

Figure 4-6. Mo 3*d* core-level HAXPES spectra of (a) Samples I, (b) II, (c) III, and (d) IV. Solid curves represent the components of 6+ (square), 5+ (triangle), and 4+ (circle) states obtained by least-square fitting. (e) Plot of area ratios of the Mo^{6+}, Mo^{5+}, and Mo^{4+}.

Hard x-ray photoemission valence-band spectroscopy

I have performed valence-band XPS measurements to understand how Mo^{5+} and Mo^{4+} contribute the electron conduction of SMM. Figure 4-7(a) shows valence-band HAXPES spectra for Samples II–IV. All of the samples exhibit two structures: a prominent peak located at E_b = 3–10 eV, derived from O 2*p*, and another smaller peak near the Fermi energy (E_F). Figure 4-7(b) shows the valence-band spectra of $MoO_{3-\delta}$ thin film [63], for comparison. When $\delta = 0$, only a prominent peak from O 2*p* was observed. On the contrary, two structures similar to the present SMM samples were observed in the valence-band PES spectrum of oxygen-vacant $MoO_{3-\delta}$. In addition, according to density function theoretical calculations for stoichiometric SMM ($\delta = 0$), the bottom of the conduction band is dominated by the 4*d*-orbital of Mo^{6+} (d^0) (Fig. 4-8). Comparing Fig. 4-8(a) with the experimentally observed valence-band spectra of $MoO_{3-\delta}$ (Fig. 4-7(b)) and the theoretically predicted band structure of SMM (Fig. 4-7), the peak near E_F can be attributed to a Mo 4*d* band composed of Mo^{5+} (d^1) and Mo^{4+} (d^2) states.

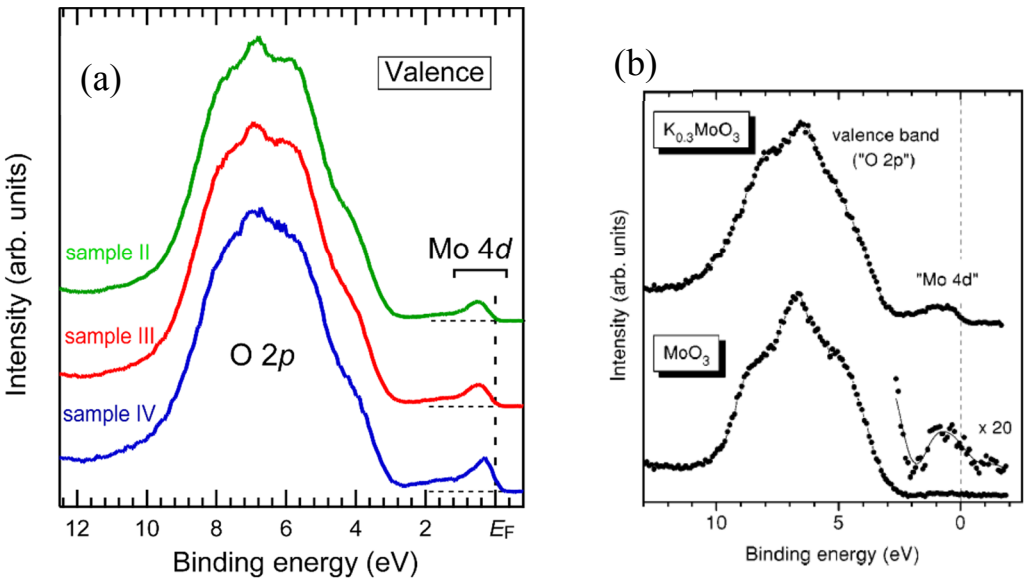

Figure 4-7. (a) HAXPES valence-band spectra of Samples II–IV near the Fermi level. (b) Valence band spectra from MoO_3 and $MoO_{3-\delta}$. Reprinted Fig. 4-7 (b) with permission from [63]. Copyright 1999 by the American Physical Society.

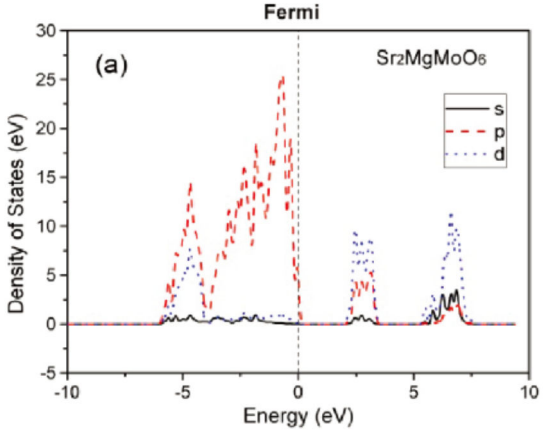

Figure 4-8. Density of states for Sr_2MgMoO_6 thin films calculated by density functional theory. Reprinted with permission from [47]. Copyright (2012) American Chemical Society.

Electric properties of oxygen-vacant SMM

Here, I discuss the electrical resistivity (ρ) of the SMM films as a function of temperature (T), as shown in Fig. 4-9(a). All samples show semiconducting behavior, The ρ(300 K) values of Samples II–IV were 6.6×10^{-2}, 5.7×10^{-2}, and 2.7×10^{-2} Ω cm, respectively, and tend to decrease with increasing δ in the samples. Notably, these resistivity values are substantially lower than those reported for polycrystalline samples synthesized by solid-state reactions, which are $> 10^{-1}$ Ω cm at 800°C. In contrast, Sample I behaved as an insulator with $\rho > 10$ Ω cm at 300 K. Figure 4-9(b) plots ρ(300 K) vs. δ evaluated from XPS. The present SMM films, particularly Sample IV, exhibit significantly low resistivity compared to polycrystalline SMM, and the resistivity is negatively correlated with the oxygen vacancy δ. This proves that electrons generated by oxygen vacancies served as carriers.

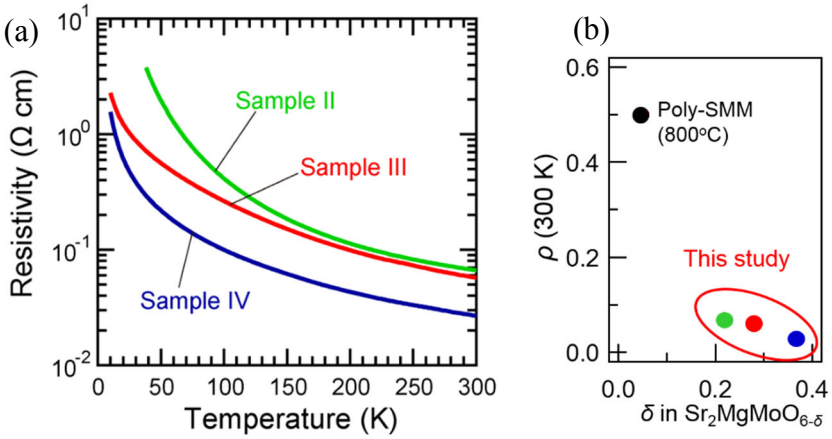

Figure 4-9. (a) Resistivity vs temperature plots for Samples II–IV at 10–300 K. (b) Resistivity at 300 K as a function of oxygen vacancies δ. Polycrystalline data [41] is also included.

Figure 4-10 plots two ρ-T curves of SMM films deposited on different substrates, STO (111) and $GdScO_3$ (110). Both showed semiconducting behavior. For SMM films on $GdScO_3$ (110) substrate, the resistivity at 300 K was the lowest, 2.1×10^{-2} Ω cm, which probably reflects the good crystallinity of SMM.

Figure 4-11 shows ln ρ vs. $T^{-1/4}$ plots for Samples II–IV in a temperature range of 100 K – 300 K. In each plot, ln ρ is proportional to $T^{-1/4}$, indicating that three-dimensional variable-range hopping (VRH) dominates the electric conduction: $\rho = \rho_0 \exp(T_0/T)^{1/4}$ [64].

In this model, the parameter T_0 is correlated with localization length α in $k_B T_0 = 18 / 3\alpha^3 N(E_F)$, where $N(E_F)$ is the density of states at the Fermi energy. Thus, smaller T_0 means larger localization length, i.e., more itinerate. For example, in case of $Sr_2Fe_{1-x}Mg_xMoO_6$ [65], the variation of T_0 with doping level is x was significant: T_0 = 4.29×10^{-4} K for metallic Sr_2FeMoO_6 (x = 0) and 3.60×10^{6} K for insulating

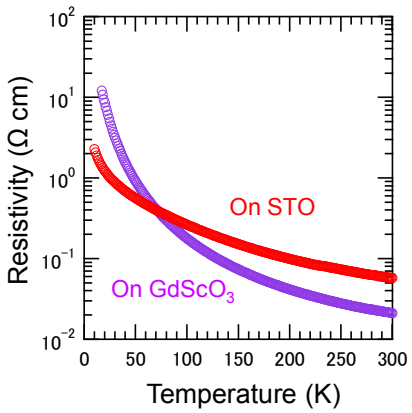

Figure 4-10. Resistivity vs temperature plot at 10–300 K for SMM films fabricated on the condition of Sample III: Comparison of STO and $GdScO_3$ substrate.

$Sr_2Fe_{0.2}Mg_{0.8}MoO_6$ (x = 0.8). In this system, both Mo 4d and Fe 3d states in B-site can contribute to the carrier conduction, whereas Mg does not have any electronic states in the vicinity of the Fermi level. Therefore increasing the amount of Mg resulted in the localization of electron carrier.

In the SMM films, the T_0 slightly decreases in the order of Sample II, III, and IV (Fig. 4-11), suggesting that the conducting electron become more itinerate with lowering ρ in SMM. This is because only Mo can contribute to the carrier conduction, thereby the localization length is supposed to be longer when the number of Mo-Mo linkage is larger, i.e., the B-site disorder is large. This scenario is consistent with the dependence of resistivity on B-site ordering ratio in Ti (d^0) - Ru (d^4) double perovskite thin film [27]. Finally, it should be noted that SMM on $GdScO_3$ substrate showed the largest T_0, i.e., the

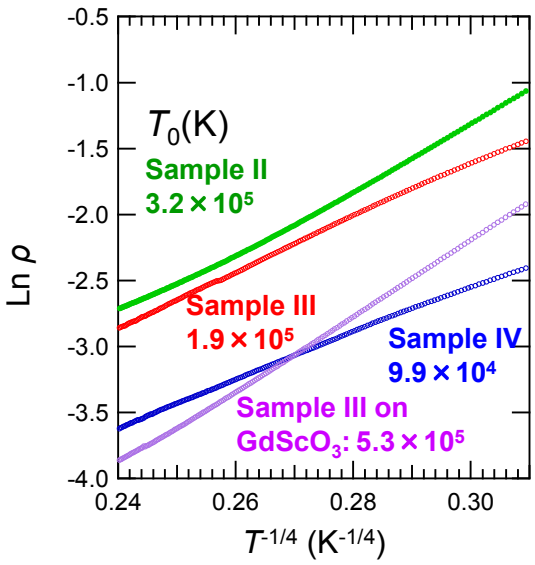

Figure 4-11. ln ρ vs. $T^{-1/4}$ plots at T = 300–100 K. T_0(K) values inside the figure are fitting of linear fitting by VRH fitting: $\rho = \rho_0 \exp (T_0/T)^{1/4}$.

carriers were most localized. There are two possible reasons. One is that BO_6 octahedrals in SMM are distorted due to epitaxial strain with orthorhombic $GdScO_3$. The other is that *B*-site disorder was decreased due to the decrease of lateral facets and/or domain boundaries because of better lattice matching with the substrate.

In conclusion, the resistivity of SMM thin film became lower because of two reasons: Carrier generation from large amount of oxygen vacancies and decrease of carrier localization caused by Mg/Mo disorder.

4.4 Summary

I characterized the electronic states and electric properties of oxygen-vacant SMM films based on x-ray photoemission spectroscopy and resistivity measurements. As a result, it was found that soft x-ray photoemission spectroscopy with Ar sputtering is not applicable to the characterization due to the presence of surface oxidized layers and the formation of Mo^0 by Ar ion-beam irradiation. On the other hand, bulk-sensitive HAXPES enabled the observation of reduced molybdenum, Mo^{5+} and Mo^{4+}. The amount of oxygen vacancy which was deduced from the peak area of Mo 3*d* was significantly larger than those reported for polycrystalline samples. Valence-band spectra exhibited Mo 4*d* states in the vicinity of the Fermi level which would supply carriers. The oxygen-vacant SMM films on STO (111) substrate showed remarkably low resistivity down to 2.7×10^{-2} Ω cm at 300 K. I have confirmed that the resistivity of SMM systematically varied with respect to the Mg/Mo ordering and δ values estimated from the HAXPES results.

Chapter 5 Conclusion and Future Perspective

In this thesis, I described thin film growth and characterization of oxygen-vacant SMM thin films fabricated by PLD which enables to grow thin films under non-equilibrium conditions.

I successfully fabricated epitaxial thin films of SMM containing a sizable amount of oxygen vacancies on $SrTiO_3$ (111) and $GdScO_3$ (110) substrates. The amount of oxygen vacancies depended on the substrate temperature and oxygen partial pressure during PLD growth. The oxygen-vacant SMM films showed larger lattice constants compared to polycrystalline samples. The XRD intensity ratio, which is a measure of the Mg/Mo ordering, was much smaller than those for bulk samples, indicating that extensive B-site disorder was introduced into the SMM films. The rocking curve suggested that SMM on $GdScO_3$ (110) samples showed better crystallinity due to better lattice matching.

In order to characterize the oxygen-vacant SMM films, I performed hard x-ray photoemission spectroscopy and resistivity measurement. Mo 3*d* photoemission spectra clearly observed the fraction of lower valence of molybdenum, Mo^{5+} and Mo^{4+}. The amount of oxygen vacancy which was deduced from the peak area of Mo 3*d* was significantly larger than those reported for polycrystalline samples. Valence-band spectra exhibited Mo 4*d* states in the vicinity of the Fermi level which supplied carriers. The oxygen-vacant SMM films on STO substrate showed remarkably low resistivity down to 2.7×10^{-2} Ω cm at 300 K. I have confirmed that the resistivity of SMM systematically varied with respect to the Mg/Mo ordering and δ values estimated from the HAXPES results.

In conclusion, I first demonstrated the fabrication of SMM thin films with high concentrations of oxygen vacancies by PLD. The SMM films showed remarkably larger extent of disorder and lower resistivity compared to polycrystalline samples. These features would be preferable as a practical SOFC components. Because PLD is not the best option for industrial processes due to the difficulty in wide-area deposition, other alternative techniques categorized into physical vapor deposition, such as sputtering, should be applied to the growth of high-quality SMM films, as the next step. This study also indicates the possibility of improving properties of *B*-site ordered double perovskites by introducing disorder in *B*-sites. There are many double perovskites which always show nearly 100% *B*-site ordered due to the large difference in two *B* site cations. It is very difficult to introduce significant amount of disorder into these double perovskites by conventional solid state reaction. Therefore, non-equilibrium techniques such as PLD would provide a chance to synthesize well-disordered double perovskites, which might exhibit novel attracting physical properties.

Acknowledgement

First of all, I would like to express my sincerest appreciation to Prof. Tetsuya Hasegawa for the opportunity for the doctoral studies and his guidance during the years. He provided me a wonderful environment for research. He always gave me warm encouragement and significant advices for my studies. He also allowed me to challenge many things including works in Advanced Leading Graduate Course for Photon Science (ALPS) program and studying abroad in Finland. It has been a pleasure studying under his supervision.

I would like to express special thanks to Dr. Akira Chikamatsu who has gently looked after me since I was undergraduate. I learned really many things including how to conduct academic research, scientific presentation, writing papers, and scientific or technical skills and know-hows. He has devoted himself to make comfortable research environment for me.

I am deeply grateful to Prof. Tomoteru Fukumura for many valuable suggestions and precious advices. His comments always brought new and deep insights of solid state chemistry. Deep appreciation also goes to Dr. Yasushi Hirose, Mr. Shoichiro Nakao, and Dr. Hideyuki Kamisaka for giving me constructive feedbacks, technical supports, and warm encouragement. All of those help me proceed this study.

I would like to appreciate Dr. Satoshi Toyoda and Dr. Eiji Ikenaga for their technical help on the x-ray photoemission experiments in SPring-8 facility and important contribution on my Ph. D course study. I also would like to appreciate Prof. Atsushi

Fujimori who was the secondary supervisor in ALPS program. Fruitful discussion with him were precious in my work.

I am deeply grateful to Prof. Maarit Karppinen and all the members in her group, Aalto University in Finland, for accepting me for studying there for three months. I was able to gain lots of priceless experience there.

I would like to thank Daichi Oka and Tomoo Terasawa, the closest peers in the chemistry department, University of Tokyo. Their energetic activities always stimulate me, in particular when I faced difficulties on my work. Many thanks also goes to all the members in Hasegawa group: Dr. Sohei Okazaki, Dr. Chang Yang, Dr. Daisuke Ogawa, Dr. Youngok Park, Anri Watanabe, Tatsunori Kawashima, Jie Wei, Shungo Kojima, Tsukasa Katayama, Atsushi Suzuki, Thantip S. Krasienapibal, Jeon Il, Xi Shen, Kazuki Aizawa, Shun Inoue, Kenta Shimamoto, Mayuko Oka, Ryosuke Sei, Kaori Kurita, Ryosuke Takagi, Tomoya Onozuka, Kenichi Kaminga, Masahito Sano, Jumpei Takahashi, Kyohei Yamatake, Vitchaphol Motaneeyachart, Keisuke Kawahara, Yuji Kurauchi, Ryota Kantake, Fahd S. Khan, Yutaka Uchida, Dai Kutsuzawa, Takuma Takeda, Takanori Yamazaki, Naoki Kashiwa, Shunsuke Shibata, Naoaki Hashimoto, and Keisuke Yamada. I would also thank the secretaries, Ms. Mie Umino, Ms. Miki Komazawa, Ms. Mayumi Kikuchi, and Ms. Aya Imoji, for their valuable supports.

Finally, I would like to express special thanks to my family for their devotion for many years.

Bibliography

[1] G. King and P. M. Woodward, J. Mater. Chem. **20**, 5785 (2010).

[2] M. T. Anderson, K. B. Greenwood, G. A. Taylor, and K. R. Poeppelmeier, Pros. Solid St. Chem. **22**, 197 (1993).

[3] A. Ohtomo, S. Chakraverty, H. Mashiko, T. Oshima, and M. Kawasaki, J. Mater. Res. **28**, 689 (2013).

[4] K. I. Kobayashi, T. Kimura, H. Sawada, K. Terakura, and Y. Tokura, Nature **395**, 677 (1998).

[5] M. García-Hernández, J. L. Martínez, M. J. Martínez-Lope, M. T. Casais, and J. A. Alonso, Phys. Rev. Lett. **86**, 2443 (2001).

[6] D. Niebieskikwiat, A. Caneiro, R. D. Sanchez, and J. Fontcuberta, Phys. Rev. B **64**, 180406 (2001).

[7] J. Navarro, B. Ll, F. Sandiumenge, M. Bibes, A. Roig, B. Martinez, and J. Fontcuberta, J. Phys.: Condens. Matter **13**, 8481 (2001).

[8] A. S. Ogale, S. B. Ogale, R. Ramesh, and T. Venkatesan, Appl. Phys. Lett. **75**, 537 (1999).

[9] T. Saha-Dasgupta and D. D. Sarma, Phys. Rev. B **64**, 064408 (2001).

[10] T. Manako, M. Izumi, Y. Konishi, K.-I. Kobayashi, M. Kawasaki, and Y. Tokura, Appl. Phys. Lett. **74**, 2215 (1999).

[11] S. R. Shinde, S. B. Ogale, R. L. Greene, T. Venkatesan, K. Tsoi, S. W. Cheong, and A. J. Millis, J. Appl. Phys. **93**, 1605 (2003).

[12] S. Kadota, Y. Matsumoto, and T. Sasagawa, Jpn. J. Appl. Phys. **50**, 01BE13 (2011).

[13] A. J. Hauser, R. E. A. Williams, R. A. Ricciardo, A. Genc, M. Dixit, J. M. Lucy, P. M. Woodward, H. L. Fraser, and F. Yang, Phys. Rev. B **83**, 014407 (2011).

[14] T. L. Meyer, M. Dixit, R. E. A. Williams, M. A. Susner, H. L. Fraser, D. W. McComb, M. D. Sumption, T. R. Lemberger, and P. M. Woodward, J. Appl. Phys. **116**, 013905 (2014).

[15] H. J. Zhao, W. Ren, Y. Yang, J. Íñiguez, X. M. Chen, and L. Bellaiche, Nat. Commun. **5**, 4021 (2014).

[16] N. S. Rogado, J. Li, A. W. Sleight, and M. A. Subramanian, Adv. Mater. **17**, 2225 (2005).

[17] M. Hashisaka, D. Kan, A. Masuno, M. Takano, Y. Shimakawa, T. Terashima, and K. Mibu, Appl. Phys. Lett. **89**, 032504 (2006).

[18] H. Itoh, J. Ozeki, and J. Inoue, J. Mag. Mag. Mater. **310**, 1994 (2007).

[19] S. F. Matar, M. A. Subramanian, A. Villesuzanne, V. Eyert, and M. H. Whangbo, J. Mag. Mag. Mater. **308**, 116 (2007).

[20] M. Hashisaka, D. Kan, A. Masuno, T. Terashima, M. Takano, and K. Mibu, J. Mag. Mag. Mater **310**, 1975 (2007).

[21] M. Singh, K. Truong, S. Jandl, and P. Fournier, Phys. Rev. B **79**, 224421 (2009).

[22] Y. Sakurai, I. Ohkubo, Y. Matsumoto, H. Koinuma, and M. Oshima, J. Appl. Phys. **110**, 063913 (2011).

[23] J. Kanamori, J. Phys. Chem. Solids **10**, 87 (1959).

[24] J. B. Goodenough, Phys. Rev. **100**, 564 (1955).

[25] S. Chakraverty, A. Ohtomo, D. Okuyama, M. Saito, M. Okude, R. Kumai, T. Arima, Y. Tokura, S. Tsukimoto, Y. Ikuhara, and M. Kawasaki, Phys. Rev. B **84**, 064436 (2011).

[26] W. E. Pickett, Phys. Rev. B **57**, 10613 (1998).

[27] K. Nogami, K. Yoshimatsu, H. Mashiko, E. Sakai, H. Kumigashira, O. Sakata, T. Oshima, and A. Ohtomo, Appl. Phys. Express **6**, 105502 (2013).

[28] S. Chakraverty, K. Yoshimatsu, Y. Kozuka, H. Kumigashira, M. Oshima, T. Makino, A. Ohtomo, and M. Kawasaki, Phys. Rev. B **84**, 132411 (2011).

[29] S. Chakraverty, X. Z. Yu, M. Kawasaki, Y. Tokura, and H. Y. Hwang, Appl. Phys. Lett. **102**, 222406 (2013).

[30] R. D. Shannon, Acta Crystallogr., Sect. A: Cryst. Phys., Diffr., Theor. Gen. Crystallogr. **32**, 751 (1976).

[31] L. Troncoso, M. J. Martínez-Lope, J. A. Alonso, and M. T. Fernández-Díaz, J. Appl. Phys. **113**, 023511 (2013).

[32] Y.-H. Huang, R. I. Dass, Z.-L. Xing, and J. B. Goodenough, Science **312**, 254 (2006).

[33] Y.-H. Huang, R. I. Dass, J. C. Denyszyn, and J. B. Goodenough, J. Electrochem. Soc. **153**, A1266 (2006).

[34] S. McIntosh and R. J. Gorte, Chem. Rev. **104**, 4845 (2004).

[35] M. Mogensen and K. Kammer, Annu. Rev. Mater. Res. **33**, 321 (2003).

[36] R. J. Gorte, J. M. Vohs, and S. McIntosh, Solid State Ionics **175**, 1 (2004).

[37] M. D. Gross, J. M. Vohs, and R. J. Gorte, J. Mater. Chem. **17**, 3071 (2007).

[38] X.-M. Ge, S.-H. Chan, Q.-L. Liu, and Q. Sun, Adv. Energy Mater. **2**, 1156 (2012).

[39] B. C. H. Steele, P. H. Middleton, and R. A. Rudkin, Solid State Ionics **40−1**, 388 (1990).

[40] D. Marrero-López, J. Peña-Martínez, J. C. Ruiz-Morales, D. Pérez-Coll, M. A. G. Aranda, and P. Núñez, Mater. Res. Bull. **43**, 2441 (2008).

[41] S. Vasala, M. Lehtimäki, S. C. Haw, J. M. Chen, R. S. Liu, H. Yamauchi, and M. Karppinen, Solid State Ionics, **181**, 754 (2010).

[42] D. Marrero-López, J. Peña-Martínezа, J.C. Ruiz-Moralesa, M.C. Martín-Sedeñob, P. Núñezа. J. Solid State Chem. **182**, 1027 (2009).

[43] Y. Ji, Y.-H. Huang, J.-R. Ying, and J. B. Goodenough, Electrochem. Comm. **9**, 1881 (2007).

[44] L. Zhang and T. He, J. Power Sources **196**, 8352 (2011).

[45] A. K. Dorai, Y. Masuda, J.-H. Joo, S.-K. Woo, and S.-D. Kim, Mater. Chem. Phys. **139**, 360 (2013).

[46] Z. Xie, H. Zhao, T. Chen, X. Zhou, and Z. Du, Int. J. Hydrog. Energy **36**, 7257 (2011).

[47] Z. Xie, H. Zhao, Z. Du, T. Chen, N. Chen, X. Liu, and S. J. Skinner, J. Phys. Chem. C **116**, 9734 (2012).

[48] C. Bernuy-Lopez, M. Allix, C. A. Bridges, J. B. Claridge, and M. J. Rosseinsky, Chem. Mater. **19**, 1035 (2007).

[49] A. B. Muñoz-García, M. Pavone, and E. A. Carter, Chem. Mater. **23**, 4525 (2011).

[50] D. G. Schlom, L.-Q. Chen, X. Pan, A. Schmehl, and M.A. Zurbuchen, J. Am. Ceram. Soc., **91**; 2429 (2008).

[51] L. W. Martin, Y.-H. Chu, R. Ramesh, Mater. Sci. Eng. R **68**, 89 (2010).

[52] P. R. Willmott and J. R. Huber, Rev. Mod. Phys., **72**, 315 (2000).

[53] T. Venkatesan, X. D. Wu, A. Inam, and J. B. Wachtman, Appl. Phys. Lett. **52**, 1193 (1988).

[54] M. Kawasaki, K. Takahashi, T. Maeda, R. Tsuchiya, M. Shinohara, O. Ishiyama, T. Yonezawa, M. Yoshimoto and H. Koinuma, Science **266**, 1540 (1994).

[55] International Tables for Crystallography (2006). Vol. C, ch. 6.1, pp. 554-590.

[56] S. Hüfner, *Photoemission Spectroscopy* (Springer-Verlag, Berlin, 1995).

[57] T.A. Koopmans, Physica **1**, 104 (1933).

[58] S. Tanuma, C. J. Powell, and D. R. Penn, Surf. Interface Anal. **43**, 689 (2011).

[59] E. Ikenaga, M. Kobata, H. Matsuda, T. Sugiyama, H. Daimon, and K. Kobayashi, J. Electron Spectros. Relat. Phenomena **190**, 180 (2013).

[60] H. Wadati, J. Mravlje, K. Yoshimatsu, H. Kumigashira, M. Oshima, T. Sugiyama, E. Ikenaga, A. Fujimori, A. Georges, A. Radetinac, K. S. Takahashi, M. Kawasaki, and Y. Tokura, Phys. Rev. B **90**, 205131 (2014).

[61] R. J. Colton, A. M. Guzman, and J. W. Rabalais, J. Appl. Phys. **49**, 409 (1978).

[62] H. Jalili, N. F. Heinig, and K. T. Leung, Phys. Rev. B **79**, 174427 (2009).

[63] M. Sing, R. Neudert, H. von Lips, M. S. Golden, M. Knupfer, J. Fink, R. Claessen, J. Mücke, H. Schmitt, S. Hüfner, B. Lommel, W. Aßmus, Ch. Jung, and C. Hellwig, Phys. Rev. B **60**, 8559 (1999).

[64] N. F. Mott, Philosophical Magazine, **19**, 835 (1969).

[65] F. Sher, A. Venimadhav, M. G. Blamire, B. Dabrowski, S. Kolesnik, and J. P. Attfield, Solid State Sciences **7**, 912 (2005).

[66] S. Vasala, H. Yamauchi, and M. Karppinen, J. Solid State Chem. **184,** 1312 (2011).

[67] 電気化学協会編『電気化学便覧　第4版』，丸善

[68] 応用物理学会 編，『応用物理ハンドブック　第2版』，p.444–445，丸善

[69] S. Vasala and M. Karppinen, Prog. Solid State Chem., *in press*.
(DOI: 10.1016/j.progsolidstchem.2014.08.001)

[70] A. Radetinac, K. S. Takahashi, L. Alff, M. Kawasaki, and Y. Tokura, Appl. Phys. Express **3**, 073003 (2010).

[71] H. H. Wang, G. Z. Yang, D. F. Cui, H. B. Lu, T. Zhao, F. Chen, Y. L. Zhou, Z. H. Chen, Y. C. Lan, Y. Ding, L. Chen, and J. K. Liang, J. Vac. Sci. Technol. A **19** 930 (2001).